CHARACTERIZATION OF ACOUSTIC OPTICAL FIBER SENSORS FOR LANDSLIDES MONITORING

RELATORE: Prof. Luca Palmieri

CORRELATORE: Ing. Luca Schenato

LAUREANDO: Leonardo Vianello

A.A. 2011-2012

UNIVERSITÀ DEGLI STUDI DI PADOVA
DIPARTIMENTO DI INGEGNERIA DELL'INFORMAZIONE
TESI DI LAUREA

CHARACTERIZATION OF ACOUSTIC OPTICAL FIBER SENSORS FOR LANDSLIDES MONITORING

RELATORE: Ch.mo Prof. Luca Palmieri

CORRELATORE: Ing. Luca Schenato

LAUREANDO: *Leonardo Vianello*

Padova, 23/04/2012

Abstract

In this thesis the experimental characterization of fiber optic sensors (FOS) for detection of precursory acoustic emissions in rockfall events is reported. All the FOSs work in interferometric configuration: the two our FOSs, namely fiber coil sensors (FCS), work on Mach-Zehnder interferometric configuration, while a third sensor, developed in VU University (Amsterdam), is a Fabry-Perot cavity working in Michelson configuration. FCSs consist in optical use a fiber coils, wounded on a aluminium cylindrical support, acting as sensing element. The other sensor, referred as ferrule top cantilever (FTC), consists in a Fabry-Perot micro-cavity created between a cantilever, carved on top of a ferrule, and the end face of a fiber housed within the same ferrule. When the cantilever vibrates due to acoustic emission waves, the length of the cavity changes, inducing an instantaneous variation of the reflectivity of the FP cavity, which is probed by a low-coherence laser, tuned at the quadrature point of the cavity.

A comparison between these sensors and a classical piezoelectric transducer (PZT) respond has been also performed. In particular, a methodology of investigation has been developed: the characterization have consisted in of analysing the responsivity and SNR in the frequency range of 20-100 kHz. Tests with a real block rock have also been done. The sensors were fastened with a screw on a Classic Gray Montemerlo Trachyte block and they were stimulated by the vibrations induced by a ball drop. The repeatability of the ball drop was guaranteed by the use of a steep slide.

These results,yet preliminary, show the capability of such FOSs to detection and monitoring of acoustic emission generated by rockfall activities.

Contents

Abstract iii

List of Figures vii

List of Tables ix

List of Acronyms x

1 Introduction 1

2 Sensor theory 3

2.1 Interferometer configurations 4

2.1.1 Michelson interferometer 4

2.1.2 Mach-Zehnder interferometer 5

2.1.3 Fabry-Perot interferometer 5

2.1.4 Sagnac interferometer 6

2.2 Acousto-ultrasonic sensors 6

2.2.1 Phase variation induced by acoustic emissions 7

2.2.2 PZT sensor 9

3 Characterization of FOS 11

3.1 Description of sensors 11

3.1.1 PZTs 11

3.1.2 FOSs 11

3.2 Test-bed 13

3.2.1 Buzzers 13

3.2.2 Signal Analysis 15

3.3 Sensitivity to pressure 15

3.4 Sensitivity to acceleration 21

3.5 Sensors performance 22

4 Analysis on rock block **25**
4.1 Acoustic Energy 26
4.2 Experiment n° 1 28
4.3 Experiment n° 2 34
4.4 Experiment n° 3 37

5 Conclusions **45**

A Acoustic insulation of sensors **47**

References **49**

List of Figures

2.1 Michelson and Mach-Zehnder interferometric systems. 5
2.2 Fabry-Perot and Sagnac interferometric systems. 6

3.1 Vallen Systeme instrumentation used. 12
3.2 Photos of used FCSs. 12
3.3 The buzzers used for characterize FOSs. 14
3.4 Mach-Zehnder setup used with the Fiber Coil Sensor. 15
3.5 FTC readout apparatus. 15
3.6 Photos of FTC. 16
3.7 Setup to test the pressure sensitivity of the sensors. 16
3.8 Responsivity and SNR of Air backed FCS. 17
3.9 Responsivity and SNR of Mandrel FCS. 18
3.10 Responsivity and SNR of PZT. 19
3.11 Responsivity and SNR of the sensors for 10 V_{pp} at the buzzer. . . 20
3.12 Setup for the vibrational test. 21
3.13 Vibrational test: responsivity and SNR of Air and Mandrel type sensor. 22
3.14 Comparison between pressure and vibrational test. 23

4.1 Scheme of the rock block and holes position (unit: cm). 26
4.2 Mandrel-type FCS e FTC that has been made rugged for rock tests. 26
4.3 Repeatibility of the signal recorded by the FCS. 29
4.4 Typical ball signal response of Mandrel FCS. 29
4.5 Typical ball signal response of FTC sensor. 30
4.6 Comparison of FCS signals with silicon grease in two different days, considering same launch direction. 33
4.7 Results of $< B > / \max(< B >)$ parameter with sensors at center hole. 39
4.8 Results of SNR parameter with sensors at center hole. 40
4.9 Results of $< D > / \max(< D >)$ parameter with sensors at center hole. 41
4.10 Results of parameter of PZT on pedestal at center hole. 42

4.11 Results of parameter of FCS with ring at center hole. 43

A.1 Setup of acoustic insulation test. 48
A.2 Results of acoustic insulation. 48

List of Tables

3.1 FCSs specifications. 13

4.1 Results of Experiment n°1, with and without the use of silicon grease on FCS and FTC sensors. 31
4.2 D results of Experiment n°1, for different threshold. 32
4.3 B and SNR in Experiment n°2: results of one session of measurement. 35
4.4 D results of Experiment n°2, for different threshold. 36

List of Acronyms

AE acoustic emission

AOM acousto-optic modulator

DSO Digital Signal Oscilloscope

FP Fabry-Perot

FBG fiber Bragg gratings

FCS fiber coil sensor

FOS fiber optic sensor

FTC ferrule top cantilever

PZT piezoelectric transducer

SNR signal-to-noise ratio

WDM wavelength division multiplexing

Chapter 1

Introduction

In 1966 Kao and Hockham firstly introduced the use of optical fibers for telecommunication [1]: nowadays laser sources, optical fibers and optical amplifiers are the foundation of modern global network infrastructure. In 1967, almost simultaneously, the first papers on fiber optic sensors were published [2, 3]. The first fiber optic sensor (FOS) were used to measure position and spacing in machine tools for the industry. The evolution of the optical fiber technology boosted also the technology of FOSs, especially with the introduction of single mode fibers. Nowadays, optical fiber properties nearly reach the physical limit of the silica, so in the telecommunication field there are a lot of studies on wavelength division multiplexing (WDM), coding information and non linearity effects. On the contrary, although FOS technology is still considered emerging and a huge market penetration is not yet really started, it has a bright future ahead in several sectors due to its potential benefits [3, 4, 5]:

- greater sensitivity compared to other techniques,
- reduced size and weight,
- immunity to electromagnetic interference (EMI),
- compatibility with optical communication,
- geometric versatility for different FOS shapes,
- durability and corrosive resistance.

Potentially, there are also a lot of physical quantities that FOS can measure [5, 6]:

- acoustic, pressure and strain perturbations,

- magnetic field and current variations,
- acceleration and rotation rate,
- temperature and chemical parameters,
- length and position.

In this thesis we analyse and characterize some FOSs for acoustic-ultrasonic emission, in the framework of the project "Innovative integrated Systems for Monitoring and assessment of hIgh risk LANDslide" (SMILAND). The project, founded by Fondazione Cassa di Risparmio di Padova e Rovigo, aims at designing and implementing a FOS-based system for rockfall monitoring. Such a system could provide real-time and continuous data on vibrations induced by rock fracturing that are related to rock landslide activity. In Chapter 2 we describe the interferometric configuration and the FOSs we used, then we draw some considerations. In Chapter 3 we introduce the test results of two types of sensors sensitive to pressure waves or induced mechanical vibrations. Tests on a rock block are presented in Chapter 4, and the conclusions are drawn in the last chapter.

Chapter 2

Sensor theory

FOSs can be divided into two broad categories: *extrinsic* and *intrinsic* sensors [2, 6]. To the first category belong the sensors in which the the optical fiber is only used as a means of light transport to and from an external sensing region. On the contrary, in intrinsic fiber optic sensors, the light does not have to leave the optical fiber to perform the sensing function: in such sensors, the optical fiber itself interact with the external environment playing an active role for sensing.

Furthermore, FOSs might be categorized according to the type of fiber or the interrogation method used. For example, a multimode fiber can be used to sense pressure, temperature and also refractive index of the surrounding environment [6]. This case deals with the mechanism of radiation loss in fiber: micro bendings cause losses for pressure measure, while different refractive index of an external liquid, that replaces a piece of fiber cladding, enables the sensing of temperature or refractive index. Intensity-based single mode fiber sensor can be realized exploiting losses: for example, an acoustic sensor can be build by aligning the ends of two fibers, one of which is left free to oscillate. An acoustic wave causes the oscillation of the free fiber end, modulating the intensity of the light captured by the fixed [3].

In a single mode fiber, the phase of signal wave can be used for sensing, as well. An interferometer system works basically exploiting this information: the light from two paths, namely sensing and reference arm, interferes accordingly to the difference in length of the two paths. There are various configurations based on different setups of the arms and on different actuator [2, 3, 6]. The most known follow:

- Michelson interferometer,
- Mach-Zehnder interferometer,

- Fabry-Perot interferometer,
- Sagnac interferometer.

Other possible approaches exploit Faraday rotation and fiber Bragg gratings (FBG) [2, 5, 6]. The first one is based on Faraday's effect in optical fiber. The current that flows in an high voltage power line can generate enough magnetic field to cause the rotation of the polarization of the light that propagates in a fiber coiled around the line. With an opportune polarization setup, the physical relation between current I and phase constant β can be used to measure the current.

The FBG sensors are optical fibers with a periodic perturbation of refractive index of the core for few millimeters upto few centimeters. The refractive index perturbation and its period lead to the reflection of light in a narrow range of wavelength that satisfy the Bragg condition $\lambda_B = 2 \cdot n \cdot \Lambda$, where λ_B is the vacuum length, Λ is the grating period and n is the effective refractive index of the fiber. In this type of sensors the grating zone is the effective sensor, because the reflective wavelength depends on the grating period that may change with temperature, pressure and strain. So FBG sensors are typically used for this physical quantities. Optical integration and capability of being multiplexed represent key features for this sensor technology because they allow for the FBG for being used for distribute sensing, by writing different gratings, i.e. working at different wavelength, along the same fiber.

2.1 Interferometer configurations

Description of some FOS interferometric configurations follows.

2.1.1 Michelson interferometer

Michelson interferometer works in reflection by making the ends of the fibers of the reference and sensing arm reflective, as you can be seen in Figure 2.1a. So the light returns to the coupler after it has been modulated in the sensing arm, and it beats with the light returned from the reference arm. Consequentially the light in the sensing arm interacts twice with the environment before getting detected. The external parameter influences the length of the sensing arm, so the phase difference results generally as Eq.(2.3); thus, the intensity variation measured is described by Eq.(2.11). A benefit of this configuration is that the reference arm

can be spatially separated from the other one, and it allows for pressure, force, vibration, temperature and acoustic measurement. Michelson configuration can also measure refractive index changes with different reflection coatings.

2.1.2 Mach-Zehnder interferometer

This configuration works similarly to Michelson's one but it comprises an additional 50/50 coupler. If coupler has four ports, two signals are considered as Figure 2.1b, otherwise only one signal is analysed with a three ports coupler. The phase information obtained is given by Eq.(2.11), with cosine or sine function depending on which setup is used. Mach-Zehnder interferometer doesn't work in reflective mode, so it isn't vulnerable to spurious interference from unwanted or not perfect reflections. On the other side the light propagates inside the sensing arm once, interacting with the environment before getting detected only one time. In some case Mach-Zehnder is preferred to Michelson configuration although it hasn't the transmitter and receiver located in the same side. This interferometer is adopted for pressure and temperature measurement, for realizing microphones and hydrophones [2, 3, 6], but also for current measurement [5].

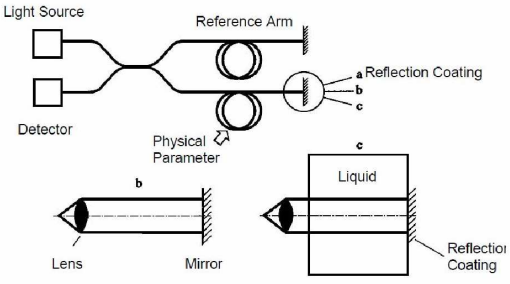

Figure 8. Fiber-optic Michelson-interferometer:
a) both ends silvered,
b) external mirror,
c) fluid in test arm.

(a) Michelson interferometer.

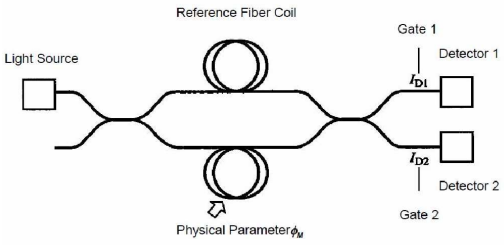

Figure 9. Fiber-optic Mach-Zehnder-interferometer.

(b) Mach-Zehnder interferometer.

Figure 2.1: Interferometric systems (from [6]).

2.1.3 Fabry-Perot interferometer

This type of interferometer is based on the transmission function of a Fabry-Perot (FP) cavity and it is shown in Figure 2.2a. It is made of a piece of fiber that has silvered ends with reflectivity close to 100 % [6]. The physical parameter changes the dimension of the cavity and it causes a different interference response,

since transmission function depends on multiple reflection inside the cavity. The reflective or the transmission signal can be analyzed in a similar way of that done for Mach-Zehnder or Michelson interferometer.

2.1.4 Sagnac interferometer

The main use of this interferometer is for rotation rate sensing [2, 6]. As shown in Figure 2.2b, the signal emitted by the laser is splitted into two waves using a beam splitter or a coupler. Both waves pass a fiber coil in opposite directions and then return to the beam splitter where they interfere. If the system does not rotate, the two waves have equal propagation time; instead if it does, the wave, moving in the same direction of it, has a slightly different propagation time because it needs more time to complete the loop respect to the other wave. So a phase difference that depends on rotation rate, fiber length and coil radius can be calculated by the time difference. Gyroscopes are the principal application of this interferometer, but FOSs for acoustic emission have been also proposed [3].

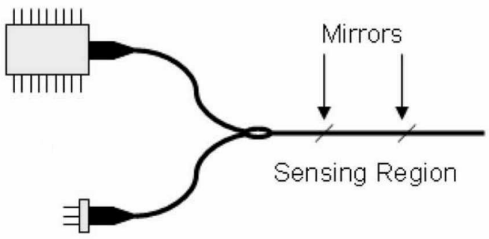

(a) Fabry-Perot interferometer.

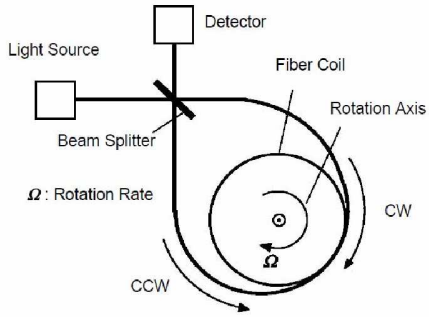

Figure 6. Fiber-optic rotation rate sensor.
CW: clockwise.
CCW: counterclockwise.

(b) Sagnac interferometer.

Figure 2.2: Interferometric systems (from [3, 6]).

2.2 Acousto-ultrasonic sensors

As stated before, acoustic emission (AE) is a physical phenomena that interferometric configurations can detect. AE is commonly defined as a transient elastic waves within a material, caused by the release of localized stress energy [1]. Hence,

[1]Ref.: http://en.wikipedia.org/wiki/Acoustic_emission

an event source is the phenomenon which releases elastic energy into the material, which then propagates as an elastic wave. Events that generate AE are various [3]:

- materials degradation: crack advance, plastic deformation surface degradation including corrosion and dis-bonding of coatings,
- reversible processes: melting or solidification, thermoelastic effects, friction between surfaces,
- fabrication processes: welding noise, grinding, drilling,
- leak and flow: flow of fluids and particles, leaks, gas evolution, boiling.

So AEs can be detected in a wide frequency ranges from under 1 kHz to several MHz: the event type and material in which they propagate define the frequency span of interest.

In our case, vibrations induced by rock fracturing are the event to detect, and according to the literature [7, 8], the most proper range of investigation spans from 20 to 100 kHz.

Now, we describe how AEs are detected using phase information obtained from interferometric configuration.

2.2.1 Phase variation induced by acoustic emissions

The phase of a signal that propagates in an optical fiber with length L is given by:

$$\phi = \beta L \tag{2.1}$$

where β is the propagation constant; furthermore it holds:

$$\beta = n_{eff} k_0 = \frac{2\pi n_{eff}}{\lambda_0} \tag{2.2}$$

where n_{eff} is the effective refractive index of travelling mode, and λ_0 is the wavelength in vacuum of the signal. When fiber is used as acoustic sensor, external acoustic waves induce phase variation that changes the interference response. From Eq. (2.1), the change in phase can be achieved by changing in length and/or in propagation constant. So it holds:

$$\Delta\phi = \beta\Delta L + L\Delta\beta. \tag{2.3}$$

Length variation is related to the local axial strain ε induced by the acoustic waves according to [3]:

$$\Delta L = \varepsilon L. \tag{2.4}$$

The variation of propagation constant $\Delta\beta$ depends on a change in the refractive index Δn and a change in fiber diameter ΔD. Accordingly:

$$\Delta\beta = \frac{\partial\beta}{\partial n}\Delta n + \frac{\partial\beta}{\partial D}\Delta D. \tag{2.5}$$

The $\partial\beta/\partial D$ term is negligible especially in single mode fiber al 1550 nm, so the dependence of diameter variation can be dropped. From Eq.(4.2) it immediately follows that:

$$\frac{\partial\beta}{\partial n} = k_0 = \frac{\beta}{n}. \tag{2.6}$$

The change in refractive index is strongly related to the strain-optic effect of a material [3, 9] and can vary significantly. From this effect, the change in the optical indicatrix [2] $(1/n^2)$ due to an applied strain can be related to the variation of refractive index as:

$$\Delta\left(\frac{1}{n^2}\right) = -2\frac{\Delta n}{n^3}. \tag{2.7}$$

Given the fiber isotropic and homogeneous and assuming there is no shear strain, the refractive index due to an applied longitudinal strain can be expressed as

$$\Delta n = -\frac{1}{2}n^3\left[\varepsilon(1-\nu)p_{12} - \nu\varepsilon p_{11}\right] \tag{2.8}$$

where ν Poisson's ratio of the fiber core. Finally, the change of phase is given by:

$$\Delta\phi = \varepsilon\beta L - \frac{1}{2}\varepsilon\beta L n^2[(1-\nu)p_{12} - \nu p_{11}]. \tag{2.9}$$

In literature, some authors [4, 10] invoke Doppler effect to explain phase variation, considering only the length variation of a flexible guide, i.e. the optical fiber, moving and vibrating in presence of AEs. The relation that links the frequency shift (Doppler frequency) to the instantaneous change of length is given by:

$$f_D = -\frac{n_{eff}}{\lambda_0}\cdot\frac{dL}{dt}. \tag{2.10}$$

[2]Indicatrix is a tri-dimensional representation of refraction index and vibration direction, where radii are the refraction indices that it's used on crystals studies. The general relation of indicatrix depends on strain-effect and electro-optic effect, but in our case there is only the first effect:

$$\Delta\left(\frac{1}{n^2}\right)_i = \sum_{k=1}^{6} p_{ik}S_j + \sum_{j=1}^{3} r_{ij}E_j$$

where p_{ik} is the strain-optic tensor, S_j is the strain vector, r_{ij} is the electro-optic tensor and E_j is the electric field component of the propagating signal.

Obviously, the previous relation provides the same first term of Eq.(2.3) without radiant normalization. From Eq.(2.9) it can be seen that external acoustic waves affect both terms, so that, from a practical point of view, it is hard to distinguish the two terms.

When a Mach-Zehnder configuration is used, the phase variation is related to the intensity $I(t)$ of the detected signal according to:

$$I(t) = I_0 \left[1 + \cos(\Delta\phi(t))\right]. \tag{2.11}$$

The relation that links the intensity $I(t)$ to the output current of the photodiode $I_p(t)$ is given by:

$$I_p(t) = \mathcal{R}P(t) \ , \tag{2.12}$$

$$P(t) = \frac{\beta}{2\omega\mu_0}|E(t)|^2 = \frac{\beta}{\omega\mu_0}I(t) \tag{2.13}$$

where $P(t)$ is the optical power, ω is the angular frequency of optical carrier, μ_0 is the magnetic permeability constant and $\mathcal{R}$ is the responsivity of photodetector.

2.2.2 PZT sensor

Currently, AEs are detected by piezoelectric transducers (PZTs) that exploit piezoelectric effect of the constitutive active material.

Piezoelectricity is a linear electromechanical interaction between the mechanical and the electrical state in crystals without a center of symmetry. The direct piezoelectric effect is present when a mechanical deformation of the piezoelectric material produces a proportional change in the electric polarization of the material, i.e. electric change appears on certain opposite faces of the piezoelectric material when it is mechanically loaded. The converse piezoelectric effect means that mechanical stress proportional to an acting external electric field is induced in the piezoelectric material, i.e. the material is deformed when an electric voltage is applied [11].

So, sensors can be made with direct piezoelectric effect, while acoustic emissions can be produced with converse piezoelectric effect. In this case, sensors are called PZTs, whereas the devices that produce AEs are called buzzers. During some of the tests we have used buzzers to induce AEs and calibrated PZTs as sensor reference.

PZTs and buzzers can be divided according to the material used for the active part and to the working frequency. There are two main groups of materials that are used for piezoelectric sensors: piezoelectric ceramics and single crystal

materials. The ceramic materials (such as PZT ceramic) have a piezoelectric constant / sensitivity that is roughly two orders of magnitude higher than those of the natural single crystal materials. The piezoeffect in piezoceramics is "trained", so unfortunately their high sensitivity degrades over time. The degradation is highly correlated with temperature, and different sensors are used depending on working temperature [3].

The thickness of the active element is determined by the desired frequency of the transducer. A thin wafer element vibrates with a wavelength that is twice its thickness. Therefore, piezoelectric crystals are cut to a thickness that is 1/2 the desired radiated wavelength. The higher the frequency of the transducer, the thinner the active element. The primary reason that high frequency contact transducers are not produced is because the element is very thin and too fragile [4]. In general the frequency response of a PZT is like an high pass filter with a usable flat region and a resonant peak, but using electrical compensation, the frequency response can be flat on working frequency range avoiding resonance peak (see Figure 3.1b).

PZTs find application in many situations: non destructive testing, health monitoring, aerospace instrumentation, industrial process control, acoustic emission detection. Buzzers, also called piezoelectric actuators, have a lot of applications such loudspeakers, acousto-optic modulators, acoustic emission generators.

[3] Ref. Wikipedia http://en.wikipedia.org/wiki/Piezoelectric_sensor

[4] Ref. NDT site: http://www.ndt-ed.org/EducationResources/CommunityCollege/Ultrasonics/EquipmentTrans/piezotransducers.htm

Chapter 3

Characterization of FOS

In this chapter we first describe PZTs, FOSs and buzzers. Then we reported the interferometric configurations used for characterization tests and finally we report the frequency response of all sensors.

3.1 Description of sensors

3.1.1 PZTs

A PZT from Vallen Systeme GmbH © with integrated preamplifier has been used in the experiments. The PZT model is VS30-SIC-46dB with the following specifications (Figure 3.1a):

- frequency range: 25-80 kHz,
- f_{peak}: flat (see Figure 3.1b),
- wear plate: ceramics,
- gain of integral preamplifier: 46 dB.

It has to be used along with a decoupling box (model DCPL1) represented in Fig. 3.1a.

3.1.2 FOSs

The first sensor we designed and tested is made of about 100 meters of G657 fiber tightly wound on an aluminium flanged hollow mandrel. The G657 fiber type is used because it has very low bending radius., e.g. one turn of 5 mm radius at

(a) PZT VS30-SIC-46dB and decoupling box DCPL1 from Vallen Systeme GMBH used in the tests.

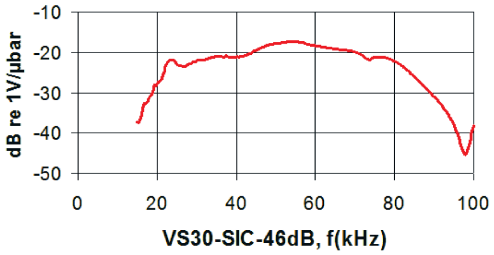

(b) The responsivity of the PZT.

Figure 3.1: Vallen Systeme instrumentation used.

1550 nm provides attenuation lower than 0.1 dB. This FOS is shown in Figure 3.2a; hereinafter we will refer to this sensor as fiber coil sensor (FCS).

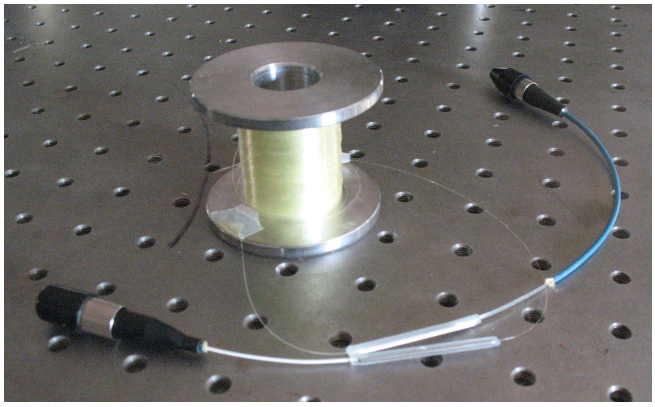

(a) Mandrel type FOS.

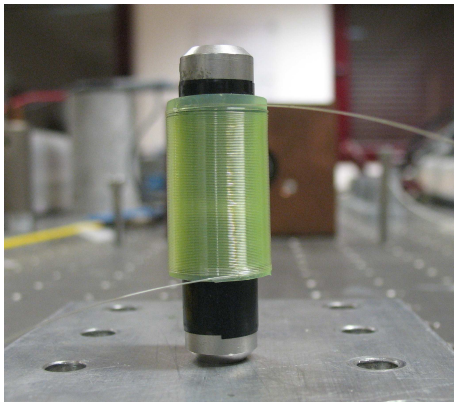

(b) Air backed type FOS without mastic.

Figure 3.2: Photos of used FCSs.

A second FOS we tested is represented in Fig. 3.2b: it is composed of about 5 m of G657 fiber coiled on plastic cylinder. The fiber is wound on a single layer. The plastic cylinder is backed on a metallic cylindric support by two o-rings. On top of the fiber, we applied a layer of glue so to increase sensibility.

All the information about these sensors are summarized on Table 3.1. These two sensors work in a Mach-Zehnder configuration.

The third sensor has been developed and produced by VU University (Amsterdam) and it is a ferrule top cantilever (FTC) obtained by carving a thin

Table 3.1: FCSs specifications.

FCS type	Sensing size (h×d) [mm]	Total size (h×d) [mm]	Fiber length [m]	n° layers
Mandrel	40×30	49×60	≈ 100	4-5
Air backed	27×17	51×18	≈ 5	1

rectangular beam out of the cleaved edge of a single mode optical fiber. The production process and a first characterization is reported in [12].

The light arrives from the fiber and then it's reflected by the cantilever, whose upper face is coated with a thin layer of gold, with different intensity depending of its vibrations; so the gap between the cantilever and the fiber end face acts as a vibration-sensitive FP cavity. The light is provide by a low-coherence laser, tuned at the manually quadrature point of the cavity.

The monolithic structure of the design eliminates any alignment procedure, and adapts well to utilization in field, even in the presence of harsh external conditions.

In this thesis we use a FTC with resonance frequency of about 12.5 kHz, but working on the dimensions of the cantilever, the spring constant k can be modified and hence also the resonance frequency f_0 according to $f_0 = 1/(2\pi)\sqrt{k/m}$, where m is the mass of the cantilever. Fig. 3.6 shows some pictures of the Ferrule Top cantilever, while in Fig. 3.5 the readout apparatus is depicted.

The reflected light is captured at receiver and the encoded signal is electrical filtered and amplified of 20 dB.

3.2 Test-bed

Before the description of the test-bed, it's necessary to briefly talk about the acoustic emission sources used on the following test.

3.2.1 Buzzers

Some buzzers have been used to induce acoustic and vibration waves. In particular the sensor have been tested for determine the pressure and acceleration sensitivity. Buzzers were driven by AC signal with frequency in the range [20-100] kHz. The pressure sensitivity has been tested by measuring the responsivity

of each sensor to acoustic waves generated in air by a buzzer, whose emission were directed to the sensor itself.

Acceleration sensitivity was measured with the following setup: a buzzer was coupled to a metal plate and a vibration was induced. Opportune insulating material covered the buzzer to absorb the acoustic wave generated in air. Sensors were screwed to the plate and the responsivity to the induced vibration was measured.

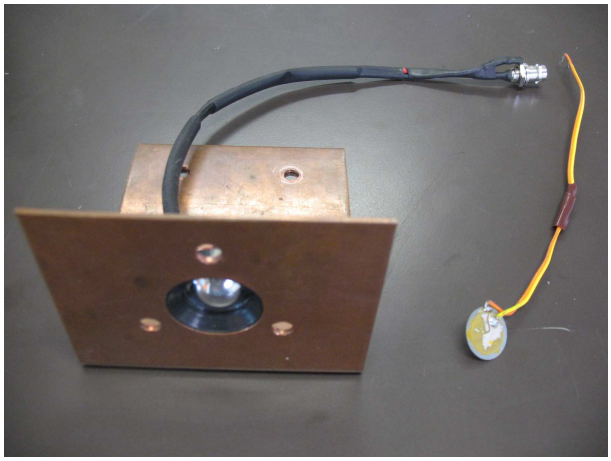

Figure 3.3: The buzzers used for characterize FOSs.

The fiber coil sensors were interrogated by means of the setup represented in Fig. 3.4.

In fig. 3.4 the light source is a high coherent DFB laser at λ_0 =1550 nm (by Koheras , with line width $>$ 2 kHz) and the reference arm of the interferometer is modulated at 40 MHz with an acousto-optic modulator (AOM). Any external perturbation acting on the fiber coil causes a variation of the fiber length, originating a modulation of the optical phase at the output of the sensing arm, which interferes with the reference signal, producing a beating signal. The presence of the AOM up-shifts the frequency of the beating around 40 MHz, far enough from the low-frequency region, dominated by amplitude fluctuations. A frequency modulated (FM) discriminator board is used to detect the instantaneous frequency shift due to the perturbation. The FM board used here is based on a doubly-balanced quadrature FM detector whose output demodulated signal is proportional to the frequency shift and it is AC-coupled, to further filter out slow signal fluctuations. A Digital Signal Oscilloscope (DSO) (Agilent DSO7054A) has been then used to digitalize the signal.

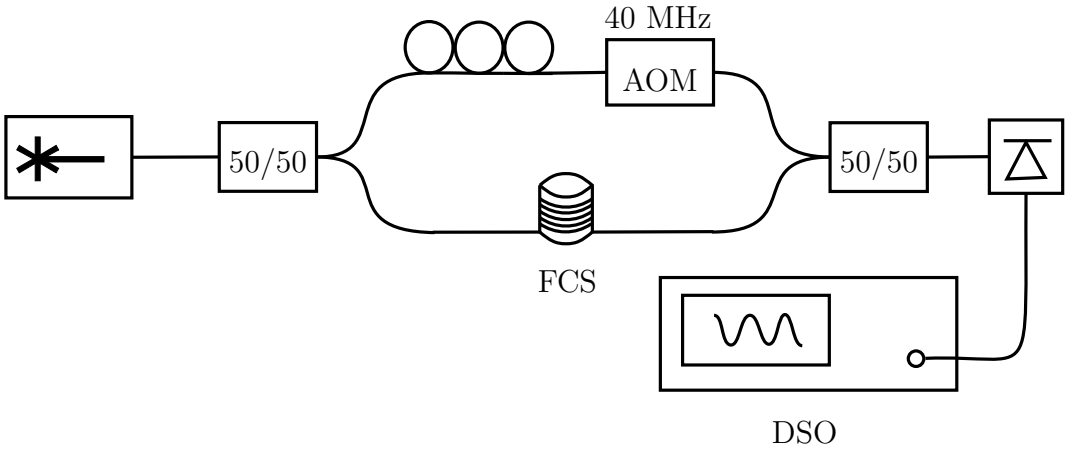

Figure 3.4: Mach-Zehnder setup used with the Fiber Coil Sensor.

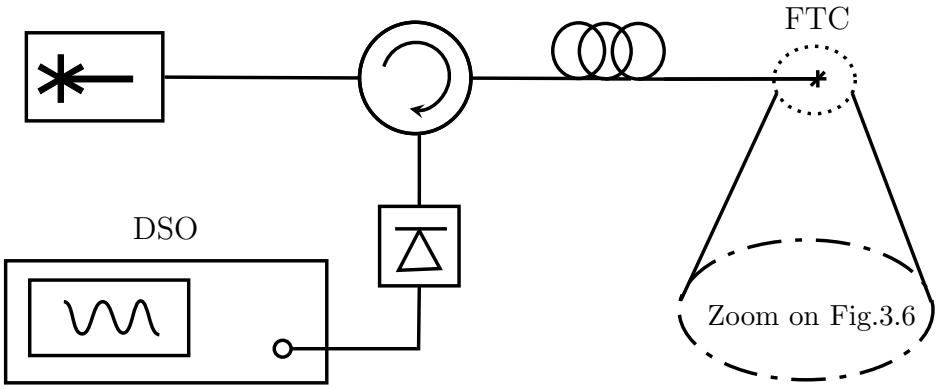

Figure 3.5: FTC readout apparatus.

3.2.2 Signal Analysis

Each sensor has been characterized in term of responsivity and signal-to-noise ratio (SNR) by varying the frequency of the perturbation signal generated by the buzzer.

3.3 Sensitivity to pressure

In this test the FOS is in front of a buzzer at several centimetres distance and a layer of insulating foam is used to isolate sensor and buzzer from external noise (see Figure 3.7). This layer also try to exclude external noise: it tries because as proved in Appendix A, the best soundproof material in the frequency range of interest is a expanded polystyrene used in certain parcel post as packaging material. So the main use of the pink soundproof is to focus the buzzer emissions.

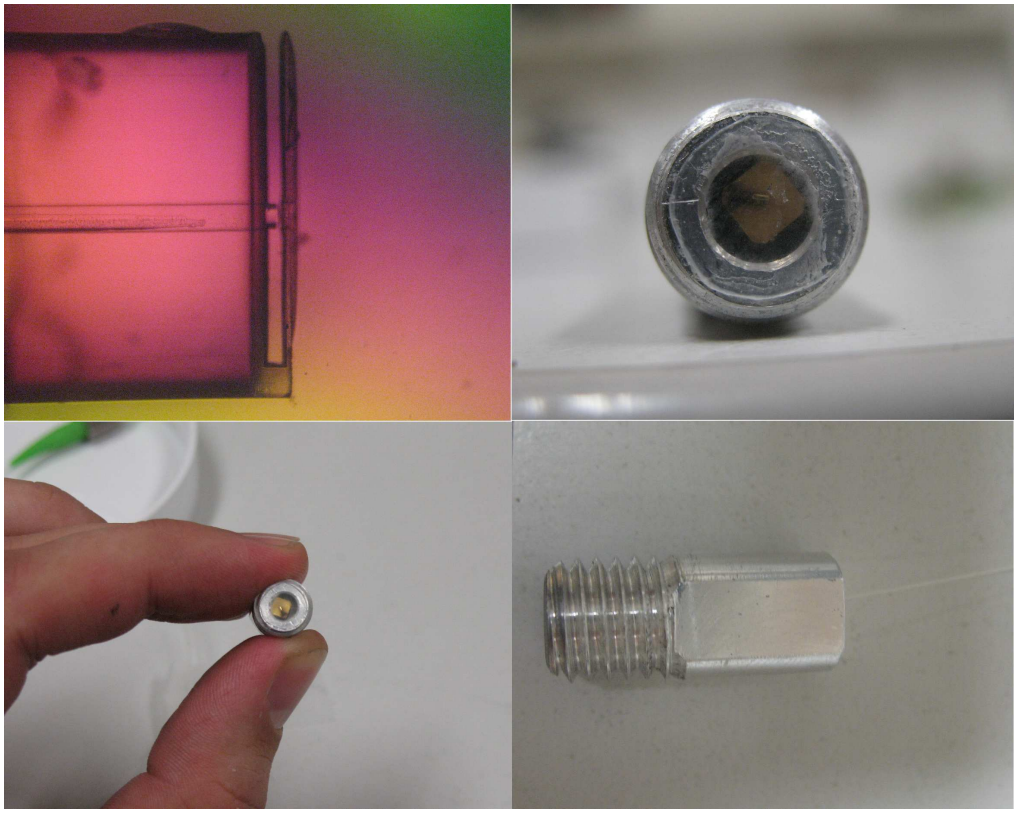

Figure 3.6: Photos of FTC.

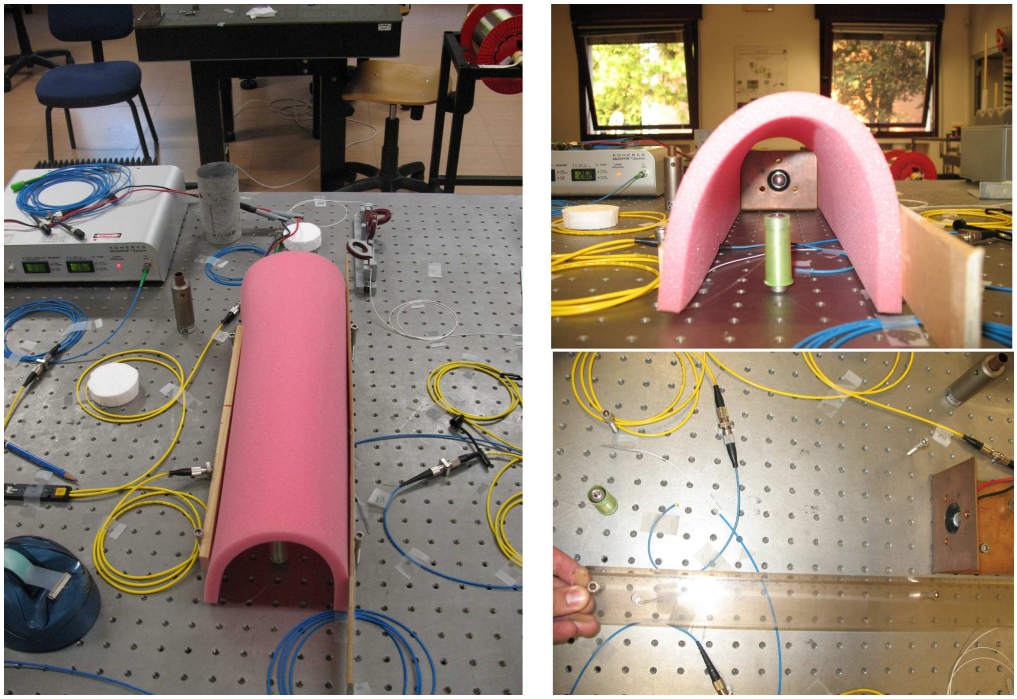

Figure 3.7: Setup to test the pressure sensitivity of the sensors.

In Figure 3.8, 3.9 and 3.10 there are the responsivity and the SNR of Air backed FCS, Mandrel FCS and PZT for two different peak-to-peak voltage (V_{pp}) at the buzzer are shown. The distance between buzzer and sensors was 34 cm.

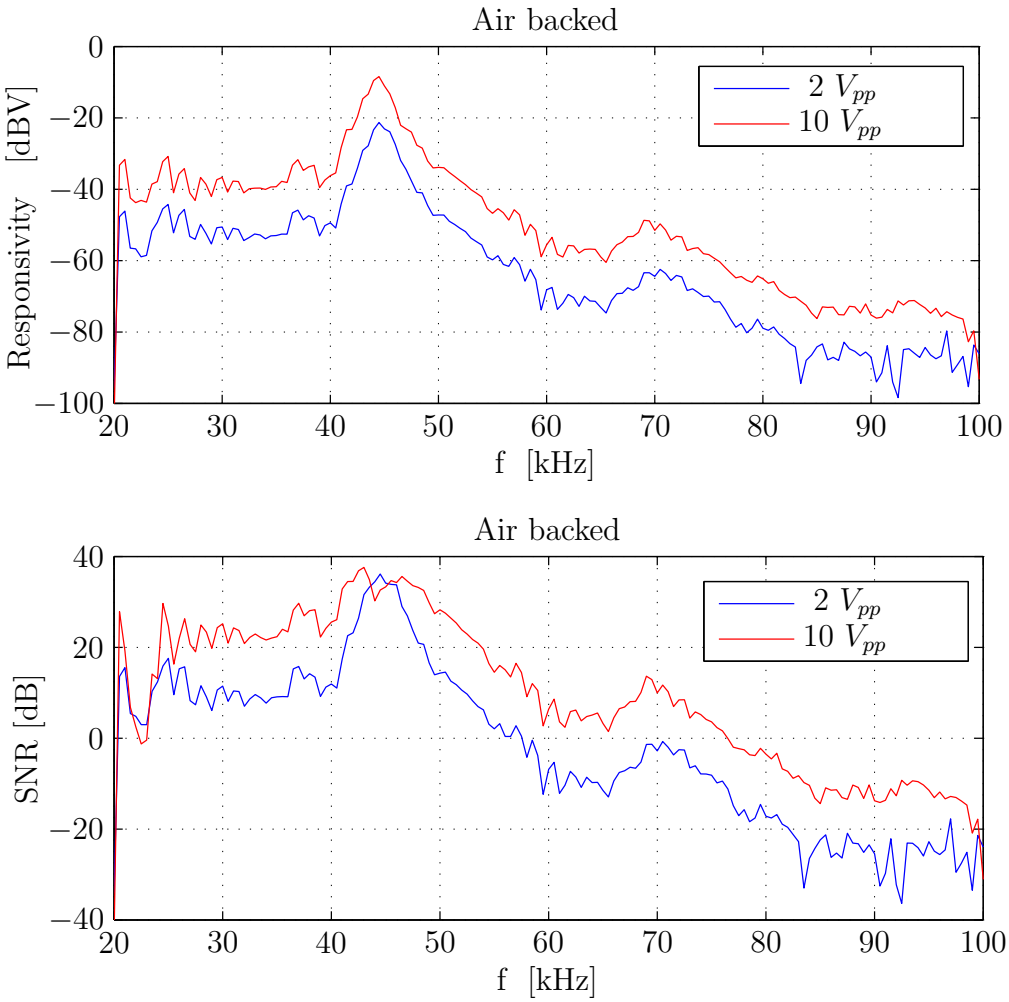

Figure 3.8: Responsivity and SNR of Air backed FCS.

Repeatability of the setup has been confirmed by repeating the measurement several time.

We may notice that an increased responsivity of 10 dB is found when the buzzer is driven with 10 V of peak-to-peak voltage.

In Figure 3.11 we compare the responsivity of the sensors when the buzzer was driven by 10 V peak-to-peak. We may notice that the air-backed FCS shows a peak in the responsivity at approx. 45 kHz and a quite flat response for smaller frequency. The mandrel-type FCS, on the contrary, exhibits a flat response for all frequency in the investigated AEs range. Finally, the PZT has the larger

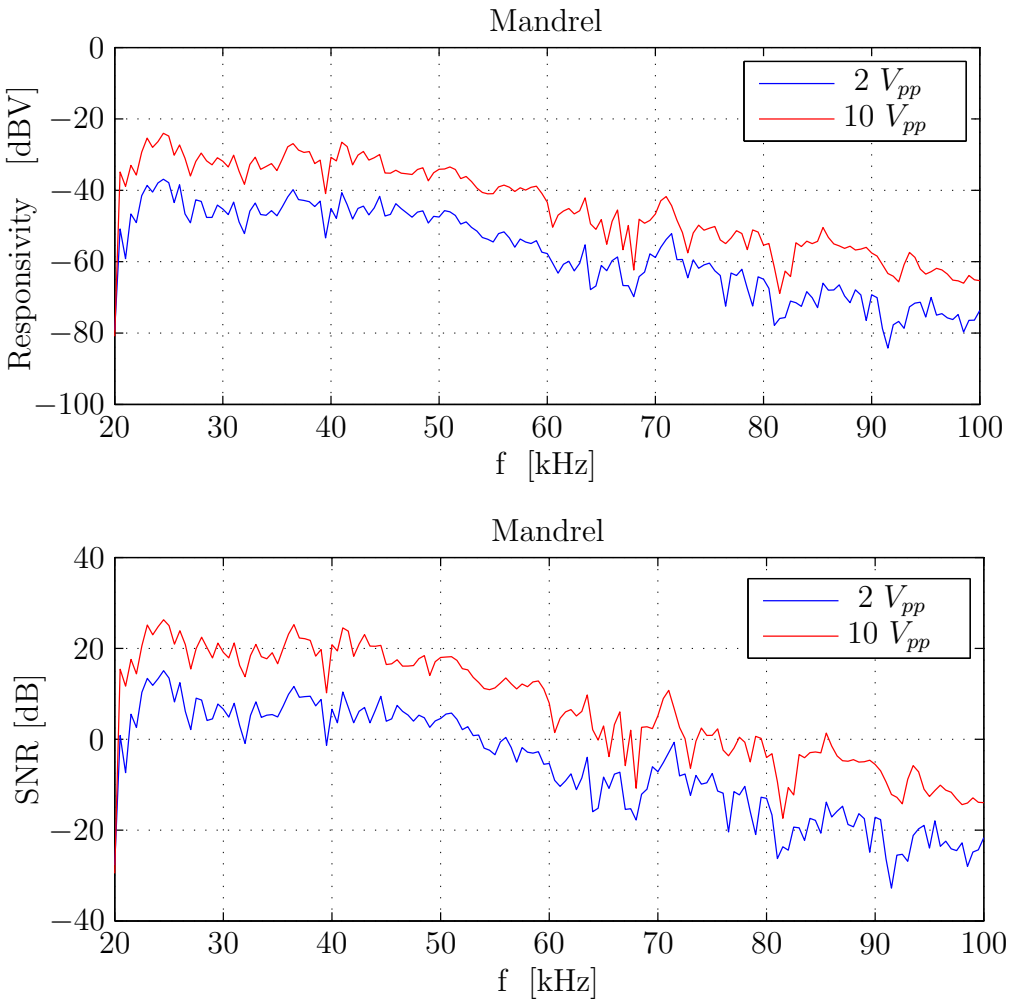

Figure 3.9: Responsivity and SNR of Mandrel FCS.

responsivity (more than 20 dB with respect to the mandrel type FCS) and shows a flat response from 20 to 80 kHz.

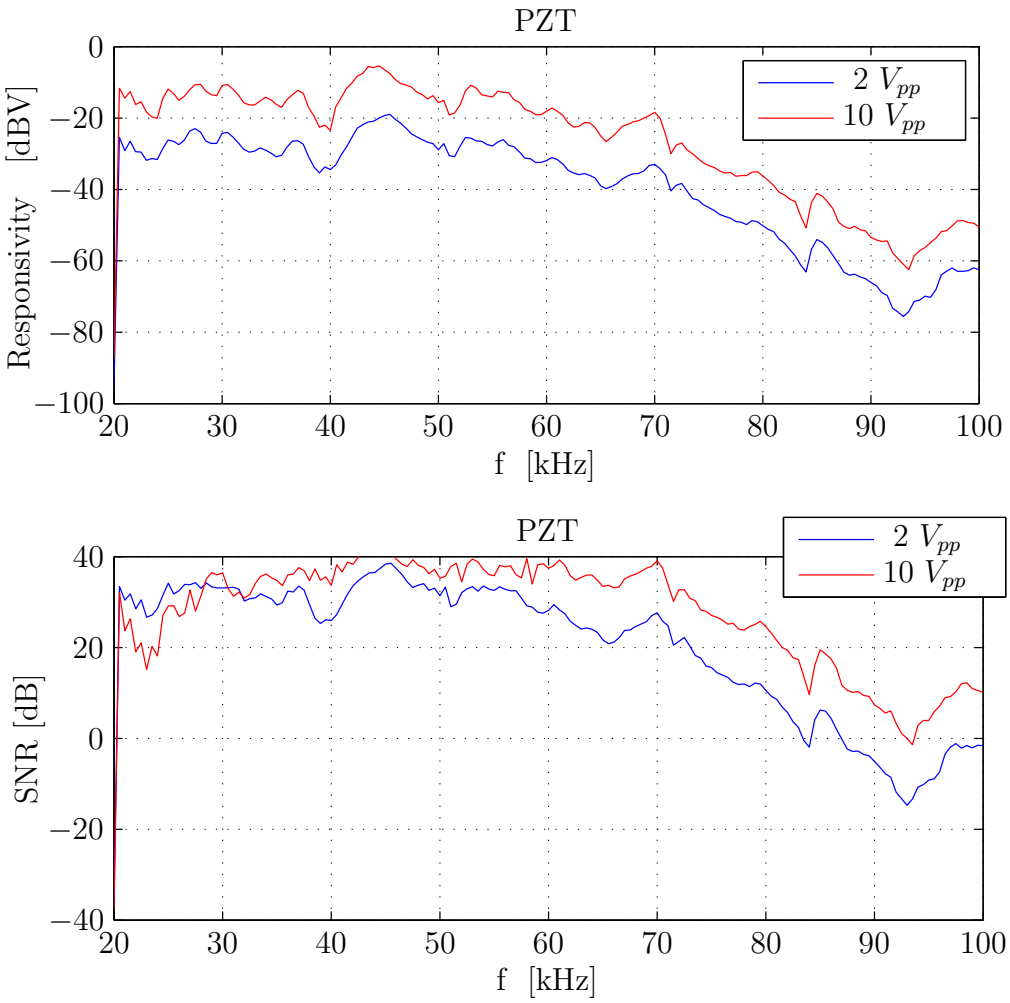

Figure 3.10: Responsivity and SNR of PZT.

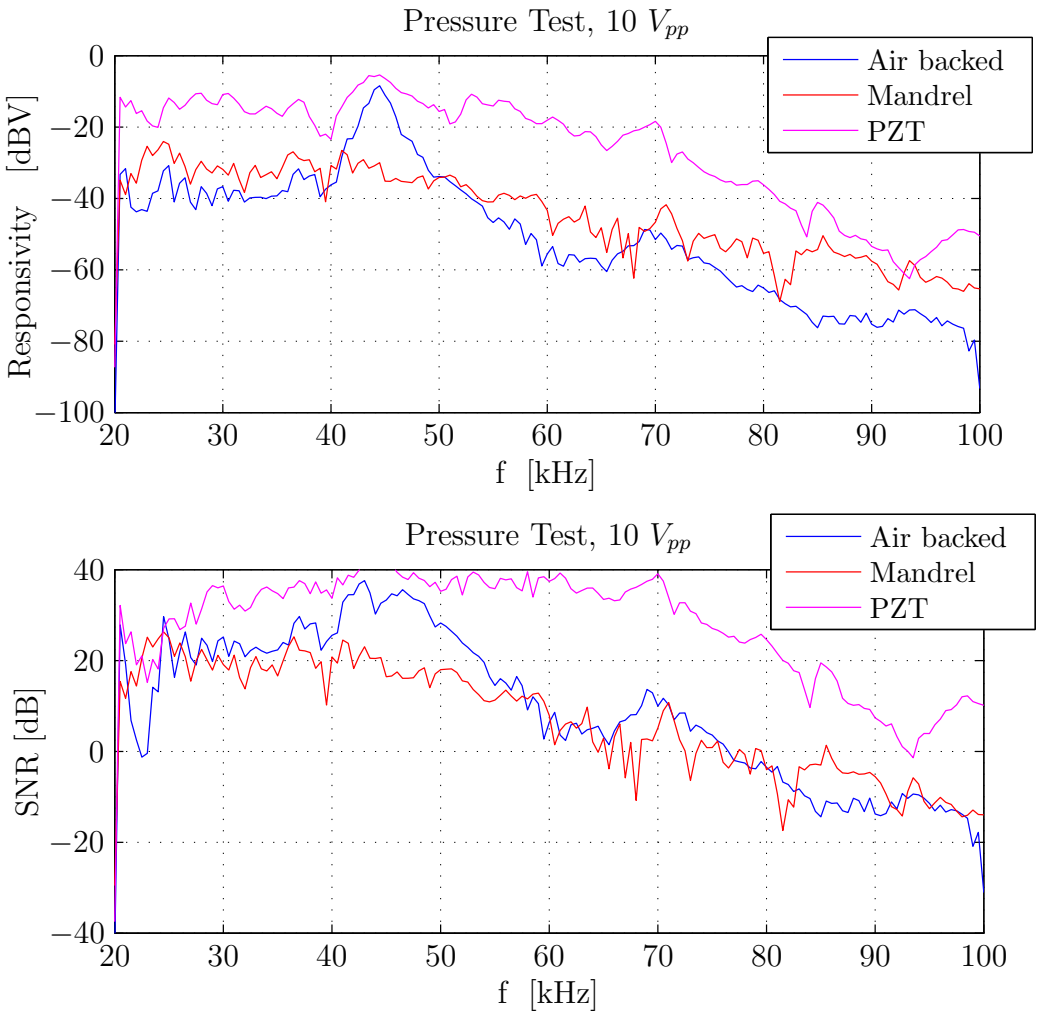

Figure 3.11: Responsivity and SNR of the sensors for 10 V_{pp} at the buzzer.

3.4 Sensitivity to acceleration

During this test a the smaller buzzer was attached on one side of a metal plate, simply supported at the two ends. On top of the buzzer we fixed an a insulating material and a polystyrene layer: a clamp is used to couple the buzzer to the plate at one side (Figure 3.12). The Air backed sensor was screwed at the other side of the plate. The Mandrel was instead achored by means of a clamp. All curves of the figures within this section are taken for 10 V peak-to-peak at the buzzer.

The result of these tests on the FOS are reported in Fig. 3.13: we have chosen to not test the PZT, given the PZT not designed for this specific application. As shown, the responsivity of the mandrel type FCS is quite flat for the entire frequency range, whereas air-backed FCS is low-pass at approx 60 kHz. Also, mandrel-type FCS responsivity is 20 dB larger on the bandpass region with comparable noise performance.

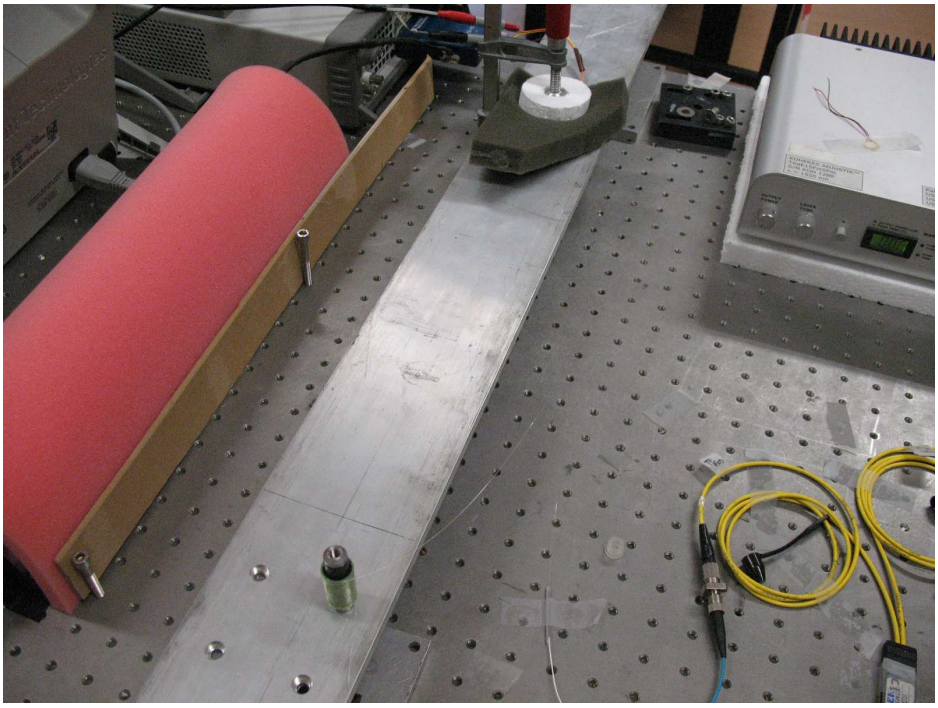

Figure 3.12: Setup for the vibrational test.

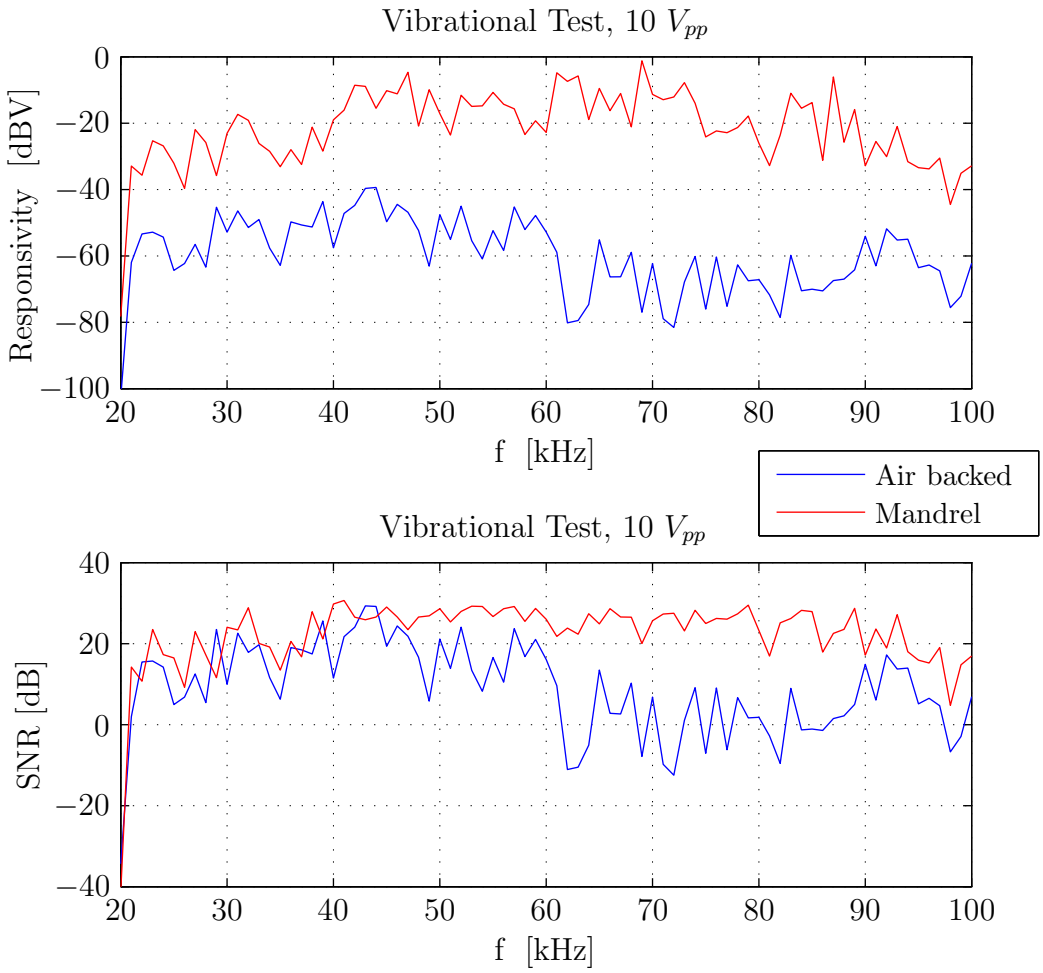

Figure 3.13: Vibrational test: responsivity and SNR of Air and Mandrel type sensor.

3.5 Sensors performance

We may notice from Figure 3.14 that Mandrel type FCS is more sensitive to acceleration rather then than pressure vibrations, while Air backed FCS is more sensitive to pressure. We think that this can be explained in term of:

- a better acoustic impedance matching of the mandrel type sensor with the vibrating metal plate for acceleration wave;
- a larger coupling surface between sensor and plate for acceleration test;
- a good acoustic impedance matching of the backed-air FCS with acoutic wave in air.

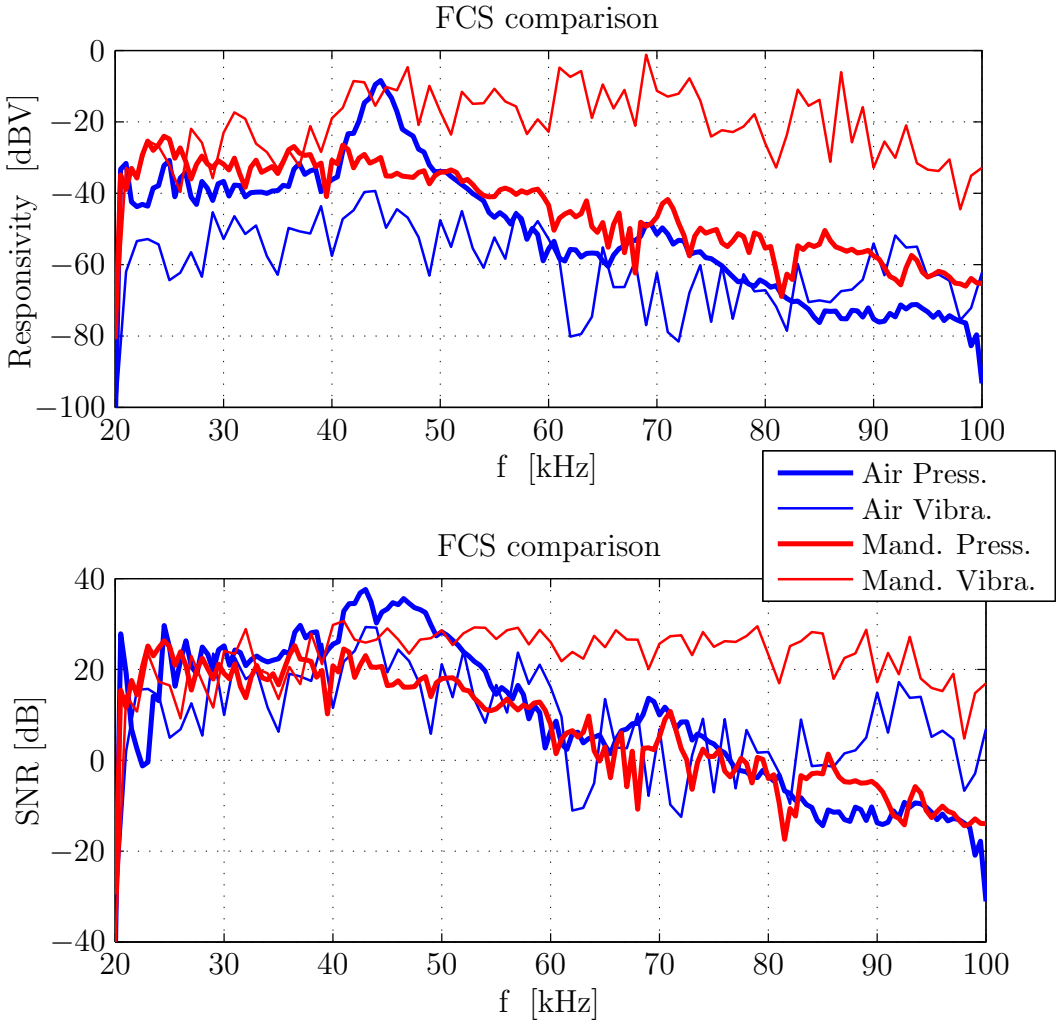

Figure 3.14: Comparison between pressure and vibrational test.

About acoustic pressure-sensitivity we also tested the sensors with different insulating material. This activity, reported in Appendix A, was aimed at determining opportune material to insulate the sensors with respect to artificial source of noise not related to crack: in fact, these FOSs are intended to be used in areas with high landslide activity and false alarms induced by acoustic noise should be avoided.

In a final analysis of this chapter, we can conclude that both FCSs are potentially capable to detect acoustic emission. Of course, responsivity and noise performance with respect to acceleration and/or pressure strongly depend on material and shape of the actuators. As a general comment, PZT performs better than FCSs in term of responsivity. About the two FCSs, the bandwidth require-

ment for this application is met only by the mandrel-type FCS, while air-backed one is low pass at 60 kHz. For this reason, the mandrel-type FCS has been chosen for the test with rock blocks.

Chapter 4

Analysis on rock block

After the characterization of the FCSs and the PZT, we now describe the various experiments realized on a Classic Gray Montemerlo Trachyte block and the signal analysis performed on the data.

It is well known that acoustic coupling plays a crucial role in the performance of AE sensors. Therefore, in order to achieve realistic coupling conditions, we have tested the sensors on a block of Classic Gray Montemerlo Trachyte ($50 \times 50 \times 15$ cm in size, about 100 kg in weight). According to the scheme in Fig. 4.1, in one of the 50×50 cm faces, we drilled 5 holes to house an internally threaded chemical anchor, to which the FOSs could be screwed. For convenience, the block was supported at 4 points near the corners of the drilled face, so that the sensors under test were housed in the bottom face of the block, while the top face was left clear allowing the excitation of AEs in different position.

The mandrel is isolated from the environment with acoustic absorbing material, and it can be fastened to the rock with a 4-cm-long M10 screw, which acts also as the main mean of acoustic coupling between the rock and the sensor. About the FTC, the sensor has been housed inside a 2-cm-long M10 bored bolt, which provides both protection and a mean of mechanical and acoustic coupling to the rock.

The purpose of these experiments is to test the Mandrel type FCS and the FTC in a more realistic scenario and possibly compare their performance to those of the PZT. Acoustic signals have been generated in a repeatable way by dropping a 5-mm-diameter steel ball along a steep slide. Signals have been acquired by a digital oscilloscope (8 bit/sample , 400 kSample/s). The repeatability of the ball impact is proved in Figure 4.3 where three consecutive Mandrel detected signals are showed [13].

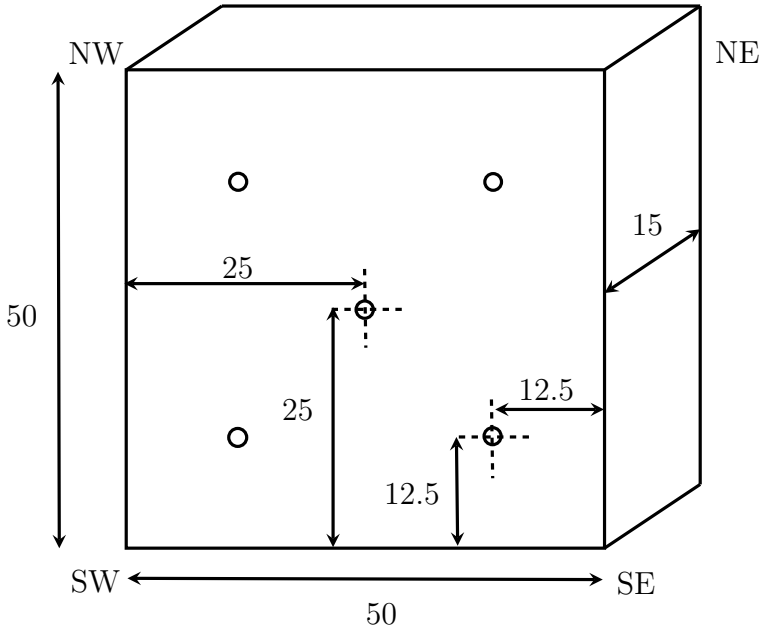

Figure 4.1: Scheme of the rock block and holes position (unit: cm).

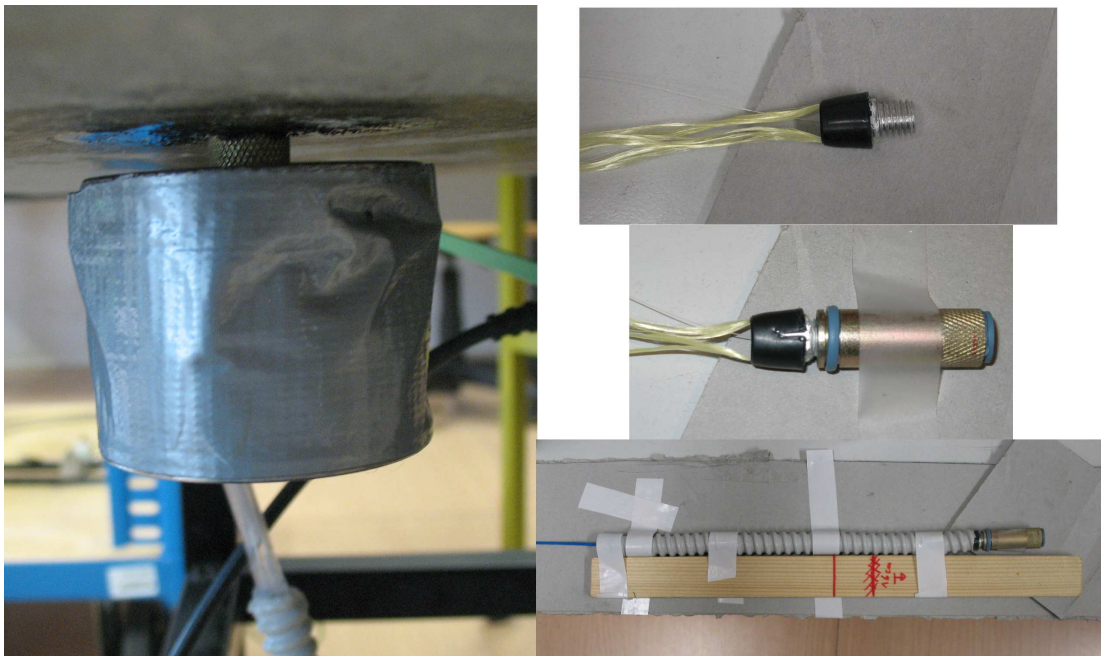

Figure 4.2: Mandrel-type FCS e FTC that has been made rugged for rock tests.

4.1 Acoustic Energy

The setup allows to acquire one event per time, triggered by the ball drop. For each signal $y(t)$ we calculate the zero-bias signal $\tilde{y}(t)$, by dropping possible bias, according to:

$$\tilde{y}(t) = y(t) - < y_{noise}(t) > \tag{4.1}$$

where $< y_{noise}(t) >$ is the mean value of the portion of the signal just before the ball drop.

For each unbiased signal, $\tilde{y}(t)$, we calculate the "acoustic energy" over an arbitrary window T as

$$\beta(\tau) = \tilde{y}^2 * \text{rect}\left(\frac{\tau}{T}\right) = \int_{\tau}^{T+\tau} \tilde{y}^2(\tau) d\tau \quad [V^2 \cdot s] \tag{4.2}$$

and define the intensity of the AE as

$$B = \max_{\tau}\{\beta(\tau)\} \quad [V^2 \cdot s]. \tag{4.3}$$

The value of T is chosen as the average length of the event. Actually, using a window longer than the event would be pointless, because it would just include more noise.

Another useful parameter is the SNR defined as:

$$\text{SNR} = 10 \log_{10}\left(\frac{B}{B_{noise}}\right) \quad [\text{dB}] \tag{4.4}$$

where B_{noise} is the B parameter calculated using $y_{noise}(t)$ instead of $y(t)$.

Accordingly, we firstly calculate the event duration D, given by:

$$D = t_2 - t_1 \tag{4.5}$$

where

$$t_1 = min\{t : \tilde{y}(t) \geq V_{th}\} \quad \wedge \quad t_2 = max\{t : \tilde{y}(t) \leq V_{th}\}. \tag{4.6}$$

The threshold V_th has been chosen as 2-3 times the standard deviation of y_noise. Another approach, more complex but robust, to calculate event duration consist in applied a similar algorithm to the envelope of the signal. After analysing the data, we set $T = 2.5$ ms for FCS and PZT, whereas for the FTC, owing to its high Q-factor, we can set $T = 50$ ms. This longer integration window results in a larger sensitivity. However, in a more realistic scenario where a sequence of AEs may occur, increasing T reduces temporal resolution.

In following sections, for each test, we summarize the minimum and maximum value of B, SNR and D, the standard deviation σ_i of SNR and D, and the deviation from the mean value μ_B defined as:

$$\mu_B = \frac{\sigma_B}{\sqrt{N}} \tag{4.7}$$

where N is the number of repetitions of the test.

4.2 Experiment n° 1

Firstly, we tested the two FOSs in the following conditions:

- FOS tightly screwed at the central hole;
- central excitation, right above the sensor.

To reduce spurious effects, the other holes have been filled with screws.

The ball was dropped in four directions (NE, NW, SW, SE) so to evaluate possible effects due to the directivity of the sensor and/or anisotropy of the rock with respect to shear waves.

The setup has been tested for repeatability by repeating the test 10 times per each direction and sensor. For example, Fig. 4.3 shows the signals corresponding to three consecutive ball drops for the FCS: as we may notice, repeatability is excellent.

Fig.4.4 and 4.5 show, for each of the two FOS, a sample signal for this setup: note that signals recorded by the FCS is quite close to the actual AE, while the FTC produces basically a dumped oscillation. It is worthwhile remarking, however, that this feature of the FTC is not at all a limitation, the bare detection and counting of AEs is enough from the present geological application. Rather the longer temporal extension of the FTC signal helps in enhancing the sensitivity, although this comes at the expense of a trade-off with temporal resolution.

In Table 4.1 intensity and SNR values of signals recorded with this setup are summarized for two cases: for sensor coupled to the rock with and without silicon grease. Silicon grease is in fact used in AE monitoring to increase the physical coupling between the rock and traditional. Indeed, we observed an improvement of the responsivity also in our FOSs; however, the SNR decreases in presence of silicon grease, probably because the higher coupling increases also the noise signal.

A large variation of the value of intensity B have been found for the two FOSs for those experimental sessions in which the sensors have been removed and then re-applied: this is due to the nature of the parameter B that is strongly dependant on the coupling, which may change depending on how tight the sensor is screwed to the block. The analysis of the responsivity corresponding to different dropping direction reveals that none of the sensor is significantly affected or that the shear wave generated by dropping the ball along different directions has negligible intensity. So far, for the current tests the sensors can be considered almost isotropic.

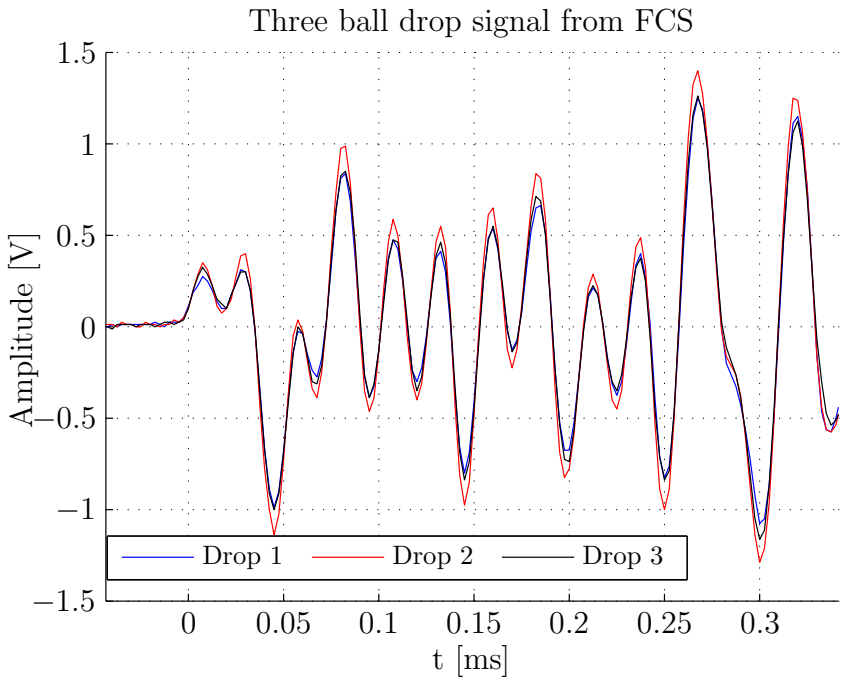

Figure 4.3: Repeatibility of the signal recorded by the FCS.

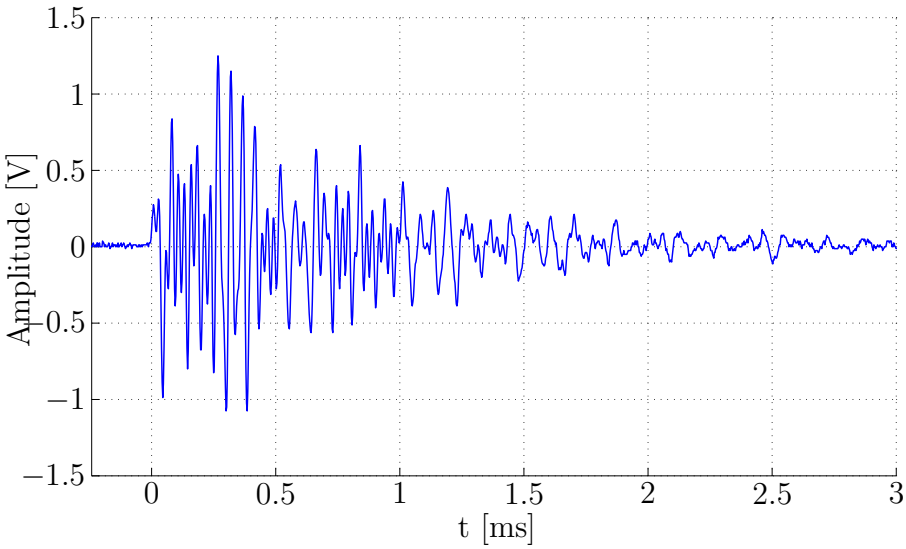

Figure 4.4: Typical ball signal response of Mandrel FCS.

In Table 4.2 the D parameter is calculated for V_thr of 5 or 10 times the σ_{noise}. As expected, higher threshold provides lower duration. The standard deviation of D is indeed often over 10% when $5{\cdot}\sigma_{noise}$ is used, as an effect of the noise, whereas smaller uncertainty in the calculated duration is observed for the larger

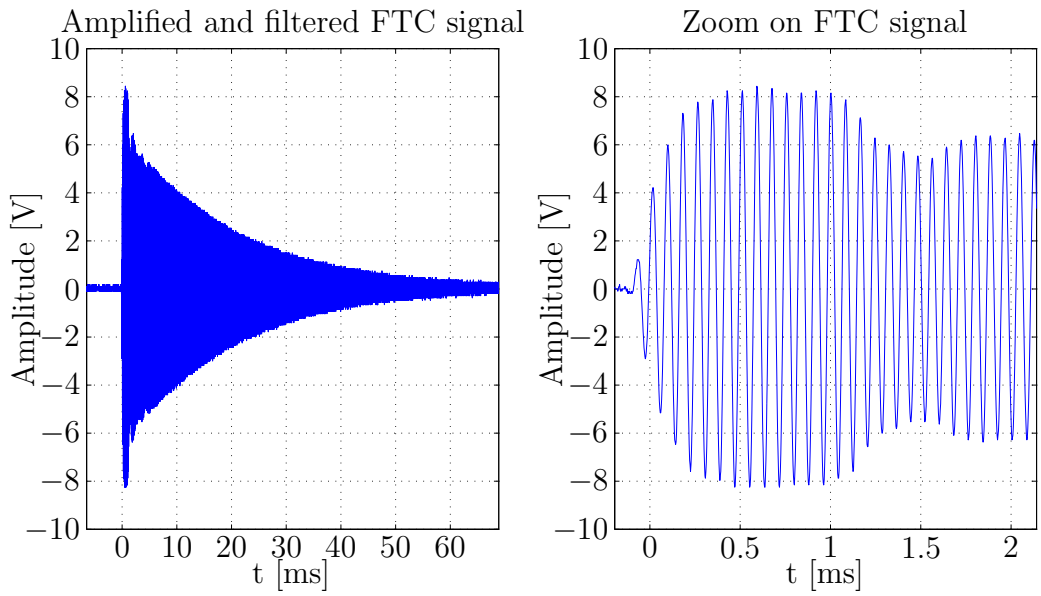

Figure 4.5: Typical ball signal response of FTC sensor.

threshold. We also note a reduced duration corresponding to the case in which Silicon grease was used.

Table 4.1: Results of Experiment n°1, with and without the use of silicon grease on FCS and FTC sensors.

	FCS without grease, T= 2,5 ms				FCS with grease, T= 2,5 ms			
	$<B>$ [mV^{2}s]	μ_B [mV^{2}s]	min(B) [mV^{2}s]	max(B) [mV^{2}s]	$<B>$ [mV^{2}s]	μ_B [mV^{2}s]	min(B) [mV^{2}s]	max(B) [mV^{2}s]
NE	200,3	8,8	161,2	245,7	225,9	15,9	154,5	325,6
SE	133,1	8,3	80,6	161,3	153,7	12,5	86,4	202,9
SW	158,1	17,6	51,4	238,0	150,9	21,3	81,9	312,3
NW	166,9	11,5	111,9	209,4	227,6	22,8	155,4	341,1
	<SNR> [dB]	σ_{SNR} [%]	min(SNR) [dB]	max(SNR) [dB]	<SNR> [dB]	σ_{SNR} [%]	min(SNR) [dB]	max(SNR) [dB]
NE	28,2	2,2	27,3	29,2	23,1	4,1	21,5	24,8
SE	27,5	3,4	25,6	28,5	21,4	5,9	19,0	22,7
SW	26,8	6,7	22,5	28,8	21,2	8,1	18,9	24,6
NW	27,6	4,2	25,7	28,9	23,0	5,9	21,6	25,1
	FTC without grease, T= 50 ms				FTC with grease, T= 50 ms			
	$<B>$ [V^{2}s]	μ_B [V^{2}s]	min(B) [V^{2}s]	max(B) [V^{2}s]	$<B>$ [V^{2}s]	μ_B [V^{2}s]	min(B) [V^{2}s]	max(B) [V^{2}s]
NE	0,202	0,005	0,170	0,220	0,114	0,007	0,076	0,140
SE	0,186	0,007	0,146	0,213	0,113	0,006	0,068	0,134
SW	0,196	0,009	0,145	0,235	0,121	0,006	0,082	0,143
NW	0,172	0,008	0,128	0,202	0,110	0,006	0,080	0,132
	<SNR> [dB]	σ_{SNR} [%]	min(SNR) [dB]	max(SNR) [dB]	<SNR> [dB]	σ_{SNR} [%]	min(SNR) [dB]	max(SNR) [dB]
NE	31,3	1,0	30,6	31,7	28,7	3,3	27,0	29,6
SE	31,0	1,7	30,0	31,6	28,7	3,1	26,5	29,5
SW	31,1	2,1	29,8	32,0	29,0	2,6	27,4	29,8
NW	30,6	2,2	29,3	31,3	28,6	2,5	27,3	29,6

Table 4.2: D results of Experiment n°1, for different threshold.

	FCS no grease, V_{th}= 5·σ_{noise}				FCS no grease, V_{th}= 10·σ_{noise}			
	D [ms]	σ_D [%]	min(D) [ms]	max(D) [ms]	D [ms]	σ_D [%]	min(D) [ms]	max(D) [ms]
NE	4,381	10,5	3,468	5,020	2,542	0,1	2,538	2,548
SE	4,628	14,4	3,533	6,105	2,540	0,5	2,503	2,548
SW	4,624	24,7	3,775	7,403	2,540	0,3	2,523	2,548
NW	4,990	28,5	3,590	8,348	2,537	0,5	2,505	2,548

	FCS grease, V_{th}= 5·σ_{noise}				FCS grease, V_{th}= 10·σ_{noise}			
	D [ms]	σ_D [%]	min(D) [ms]	max(D) [ms]	D [ms]	σ_D [%]	min(D) [ms]	max(D) [ms]
NE	2,107	16,2	1,770	2,868	1,230	2,9	1,150	1,295
SE	2,140	25,6	1,770	3,588	1,251	7,5	1,150	1,508
SW	1,973	10,4	1,690	2,203	1,204	13,6	0,848	1,508
NW	2,087	8,7	1,770	2,430	1,319	10,2	1,210	1,513

	FTC no grease, V_{th}= 5·σ_{noise}				FTC no grease, V_{th}= 10·σ_{noise}			
	D [ms]	σ_D [%]	min(D) [ms]	max(D) [ms]	D [ms]	σ_D [%]	min(D) [ms]	max(D) [ms]
NE	79,972	3,4	76,253	85,003	53,031	2,7	51,250	56,578
SE	81,531	5,7	75,840	91,320	51,634	3,2	48,250	53,250
SW	85,890	9,0	75,958	101,630	52,428	3,3	48,083	54,223
NW	91,433	26,1	74,310	153,430	50,636	3,3	47,900	52,895

	FTC grease, V_{th}= 5·σ_{noise}				FTC grease, V_{th}= 10·σ_{noise}			
	D [ms]	σ_D [%]	min(D) [ms]	max(D) [ms]	D [ms]	σ_D [%]	min(D) [ms]	max(D) [ms]
NE	82,439	26,8	69,015	138,788	46,363	5,8	41,095	49,425
SE	80,995	23,2	65,665	117,108	46,488	3,5	42,555	48,285
SW	77,289	11,6	67,028	97,140	46,976	4,2	43,058	49,438
NW	75,273	5,4	71,370	82,308	46,064	4,7	41,938	49,188

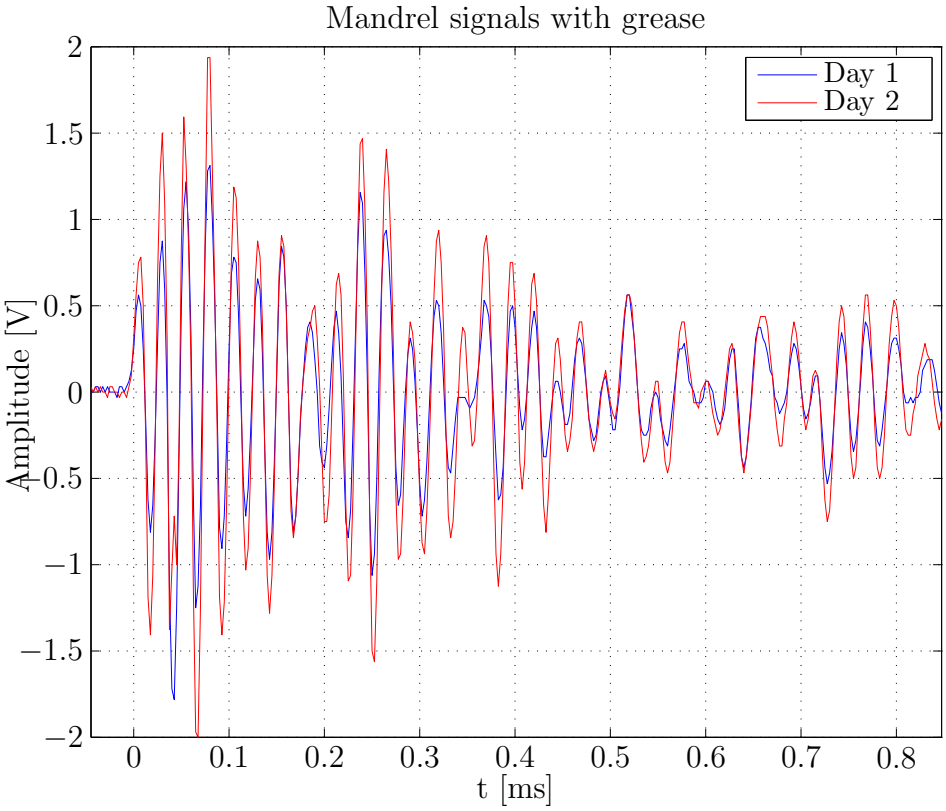

Figure 4.6: Comparison of FCS signals with silicon grease in two different days, considering same launch direction: : it appears evident that the overall evolution is the same for the two tests but the amplitude changes and that it is somehow enhanced during test of Day 2.

4.3 Experiment n° 2

In this second setup the ball is always dropped at center of the rock, while the two sensors are hosted in the holes at SW and NE, one per holes. Their reciprocal positions are swapped several times to check repeatability and find possible anisotropies on the rock. We call "Position 1" (Pos.1) the configuration with FCS at SW and FTC at NE, while "Position 2" (Pos.2) has FCS at NE and FTC at SW. The other three holes are filled by screws to exclude possible influences or resonances between the vibrations and the air cavities of the holes.

We made four sessions of measurement for Pos.1 and Pos.2, and the Tables 4.3, 4.4 report the results of one session. As notice in Experiment n° 1, the consecutive sessions denote high mean percentage difference, especially between sessions realized in different days. Again, this can be due to different coupling conditions among the different tests due to the fact that each test require the sensors to be removed and fixed again. Also, we may notice that, as expected, B decrease with the distance between sensor and point of impact, for all the sensor.

About SNR, the noise performance of the FCS are almost the same of the previous test (Table 4.1); the FTC, on the contrary, provides lower SNR in this test with respect to the previous. This is likely due to a reduced mean intensity of the detected signal in this last experiment. The FTC, in fact, seem to be more directive than the FCS: we believe that this feature of the FTC is strongly related to the coupling mechanism with respect to the FCS. We believe that the FTC, being screwed directly inside the rock, is more sensitive to volume waves. The FCS, instead is coupled both through the screw, and through one of the coil flanges directly in contact with the rock surface: this would allow for the sensor to be sensitive also to surface waves.

Table 4.3: B and SNR in Experiment n°2: results of one session of measurement.

	FCS, Pos.1, T= 2,5 ms				FTC, Pos.1, T= 50 ms			
	$<B>$ [mV^{2}s]	μ_B [mV^{2}s]	min(B) [mV^{2}s]	max(B) [mV^{2}s]	$<B>$ [mV^{2}s]	μ_B [mV^{2}s]	min(B) [mV^{2}s]	max(B) [mV^{2}s]
NE	68,0	5,9	41,2	97,2	1887,3	95,4	1437,2	2467,3
SE	48,2	7,0	10,8	86,0	1246,9	79,6	789,4	1473,4
SW	37,5	7,0	10,5	79,9	1220,7	98,0	850,2	1860,0
NW	53,8	7,1	17,3	87,5	1859,7	78,6	1497,2	2260,2
	<SNR> [dB]	σ_{SNR} [%]	min(SNR) [dB]	max(SNR) [dB]	<SNR> [dB]	σ_{SNR} [%]	min(SNR) [dB]	max(SNR) [dB]
NE	23,2	5,6	21,2	25,0	18,8	3,8	17,7	20,1
SE	21,3	12,3	15,6	24,5	16,8	6,3	14,8	17,7
SW	20,1	13,4	15,6	24,1	16,9	6,4	15,4	18,9
NW	22,0	9,4	17,6	24,4	18,8	3,2	17,9	19,6

	FCS, Pos.2, T= 2,5 ms				FTC, Pos.2, T= 50 ms			
	$<B>$ [mV^{2}s]	μ_B [mV^{2}s]	min(B) [mV^{2}s]	max(B) [mV^{2}s]	$<B>$ [mV^{2}s]	μ_B [mV^{2}s]	min(B) [mV^{2}s]	max(B) [mV^{2}s]
NE	52,0	2,7	40,0	65,8	1193,3	52,1	979,4	1461,1
SE	41,6	4,9	21,0	67,4	853,1	54,5	540,3	1083,9
SW	41,3	1,7	32,6	48,8	1165,7	42,4	1009,9	1417,5
NW	47,2	4,1	27,4	66,7	1286,1	92,8	832,6	1633,5
	<SNR> [dB]	σ_{SNR} [%]	min(SNR) [dB]	max(SNR) [dB]	<SNR> [dB]	σ_{SNR} [%]	min(SNR) [dB]	max(SNR) [dB]
NE	22,2	3,1	21,2	23,4	17,3	3,7	16,5	18,4
SE	21,0	7,9	18,3	23,3	15,7	6,0	13,8	16,8
SW	21,2	2,9	20,2	22,0	17,2	2,8	16,6	18,1
NW	21,8	5,9	19,4	23,5	17,5	6,0	15,8	18,7

Table 4.4: D results of Experiment n°2, for different threshold.

	FCS Pos.1, V_{th}= 5·σ_{noise}				FCS Pos.1, V_{th}= 10·σ_{noise}			
	D [ms]	σ_D [%]	min(D) [ms]	max(D) [ms]	D [ms]	σ_D [%]	min(D) [ms]	max(D) [ms]
NE	2,288	12,0	1,940	2,715	1,299	9,9	1,065	1,393
SE	2,507	12,1	1,708	2,923	1,228	12,9	0,980	1,393
SW	2,351	15,7	1,720	2,908	1,176	13,4	0,980	1,393
NW	2,326	10,5	2,078	2,625	1,291	11,7	1,008	1,398

	FTC Pos.1, V_{th}= 5·σ_{noise}				FTC Pos.1, V_{th}= 10·σ_{noise}			
	D [ms]	σ_D [%]	min(D) [ms]	max(D) [ms]	D [ms]	σ_D [%]	min(D) [ms]	max(D) [ms]
NE	44,334	22,7	37,743	71,878	19,128	10,1	16,708	23,315
SE	38,236	10,9	33,425	45,573	12,899	21,0	7,505	16,688
SW	38,324	22,0	31,033	60,430	13,486	17,9	10,200	18,130
NW	42,564	10,3	38,293	53,035	19,247	8,0	17,280	20,975

	FCS Pos.2, V_{th}= 5·σ_{noise}				FCS Pos.2, V_{th}= 10·σ_{noise}			
	D [ms]	σ_D [%]	min(D) [ms]	max(D) [ms]	D [ms]	σ_D [%]	min(D) [ms]	max(D) [ms]
NE	2,706	5,2	2,523	3,025	1,929	0,8	1,908	1,950
SE	2,514	10,3	2,150	2,860	1,918	0,7	1,905	1,945
SW	2,676	7,9	2,420	3,230	1,886	3,2	1,768	1,920
NW	2,738	11,0	2,398	3,535	1,924	0,8	1,910	1,948

	FTC Pos.2, V_{th}= 5·σ_{noise}				FTC Pos.2, V_{th}= 10·σ_{noise}			
	D [ms]	σ_D [%]	min(D) [ms]	max(D) [ms]	D [ms]	σ_D [%]	min(D) [ms]	max(D) [ms]
NE	37,967	11,2	31,460	44,705	15,147	11,9	13,053	18,790
SE	34,899	15,6	28,038	46,493	11,128	29,7	4,810	16,188
SW	41,062	6,2	36,273	45,303	16,222	10,6	13,665	19,330
NW	40,663	10,5	33,718	48,658	16,389	16,9	12,523	20,253

4.4 Experiment n° 3

In this experiment, we have performed several tests by dropping the ball at different positions on an uniform 7×7 grid, drawn on the top 50×50 cm face of the block. Each sensor was opportunely anchored at the center of the block. For testing the repeatability, the ball was dropped 3 times per position. Again, other holes have been filled by a steel screw and the silicon grease was used as usual.

Also the PZT was used in this experiment: it has been placed nearby the central hole. Due to its high responsivity, it has been attenuated by placing a small layer of paper in between its active face and the rock. Without this "attenuator" the signal saturated for any position the ball was dropped.

As expected, from Figure 4.7, the sensors tend to record higher amplitudes when the ball is dropped closer to the center, above their position. Nevertheless, this correspondence is not perfect, likely because of inhomogeneity in the rock sample. More interestingly, we may note that the PZT exhibits the least marked dependency on the excitation position, while the FTC the most one, and the FCS performs in between. We believe that these differences are mainly due to different sensitivity of the sensors to surface waves [1]. Actually, while the PZT is acoustically coupled to the rock only through its surface, the FTC is screwed directly inside the rock and therefore is more sensitive to volume waves. Differently, the FCS is coupled both through the screw, and through one of the coil flanges directly in contact with the rock surface. To support this argumentation, we have repeated the test installing the PZT on a pedestal made of a long flat-head bolt, screwed in the rock. In this way we reduced the direct coupling to surface waves and enhanced that to volume ones. Results of B, reported in the first graph of Figure 4.10, shows a marked increase of the dependency on the excitation position, in agreement with the hypothesis. We remark that the intrinsic insensitivity to surface waves is quite a desirable feature, for noise sources (e.g. anthropic activities and meteors) acting outside real rock masses are most likely to induce surface waves, rather than volume ones. We have noted also that the maximum B of pedestal case is greater than normal case. The reason can be the increasing of sensibility due to the insertion of pedestal, or a tighter coupling of the PZT.

To check if the surface waves may actually interact also with the FCS, we insert a metalling ring between the flange and the rock, so there is no direct

[1] In physics, a surface wave is a mechanical wave that propagates along the interface between differing media, usually two fluids with different densities. Ref. Wikipedia.

contact between rock and coil flanges and only the screw carries the vibrations. The results, reported in Figure 4.11, doesn't show a big difference in amplitude sensitivity and SNR, so we can conclude that the FCS is only marginally sensitive to surface waves.

About noise performance (Fig. 4.8), all the sensors exhibit values of SNR larger than 20 dB, with a maximum value of 35 dB for the FTC. Furthermore, PZT on the pedestal shows larger SNR than the PZT directly coupled to the rock surface; most likely, the pedestal filtered out surface waves induced by external noise sources.

Comparing the values among the sensors, the FTC shows the highest duration, while the FCS has the shortest one.

Regarding absolute performance, the FCS is the least sensitive of the three sensors. Actually, with respect to FCS, the peak intensities of FTC and PZT are about 30 dB and 50 dB higher, respectively. Notice, however, that both FTC and PZT include at the receiver an electrical amplification of 20 dB and 46 dB, respectively; differently electrical amplification is not exploited in the FCS. Taking amplification into account, the most sensitive sensor is the FTC, although we recall that this performance comes at the expense of a twentyfold reduction of temporal resolution.

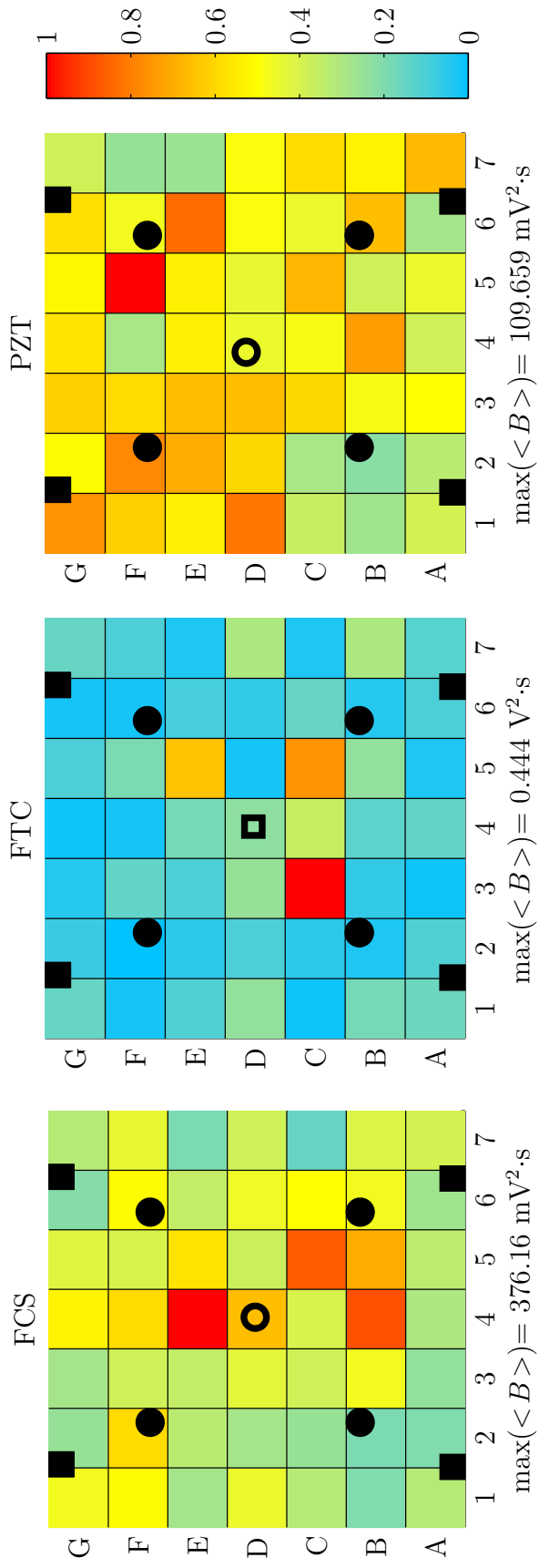

Figure 4.7: Results of $< B > / \max(< B >)$ parameter with sensors at center hole.

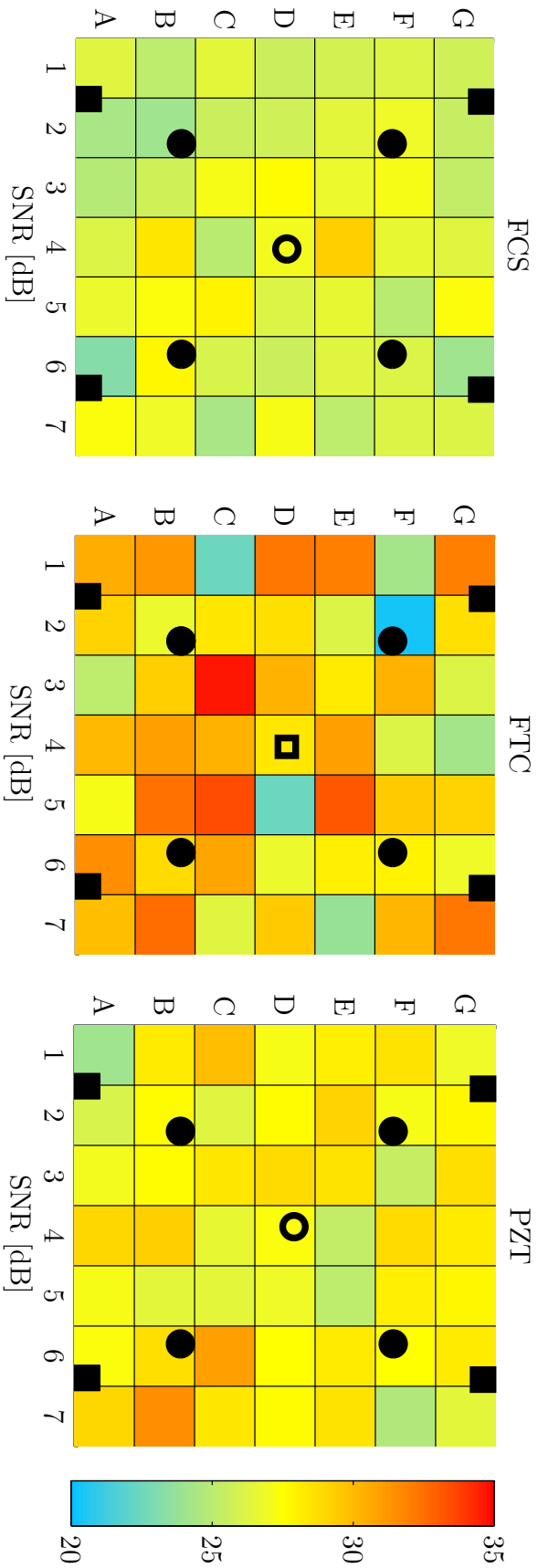

Figure 4.8: Results of SNR parameter with sensors at center hole.

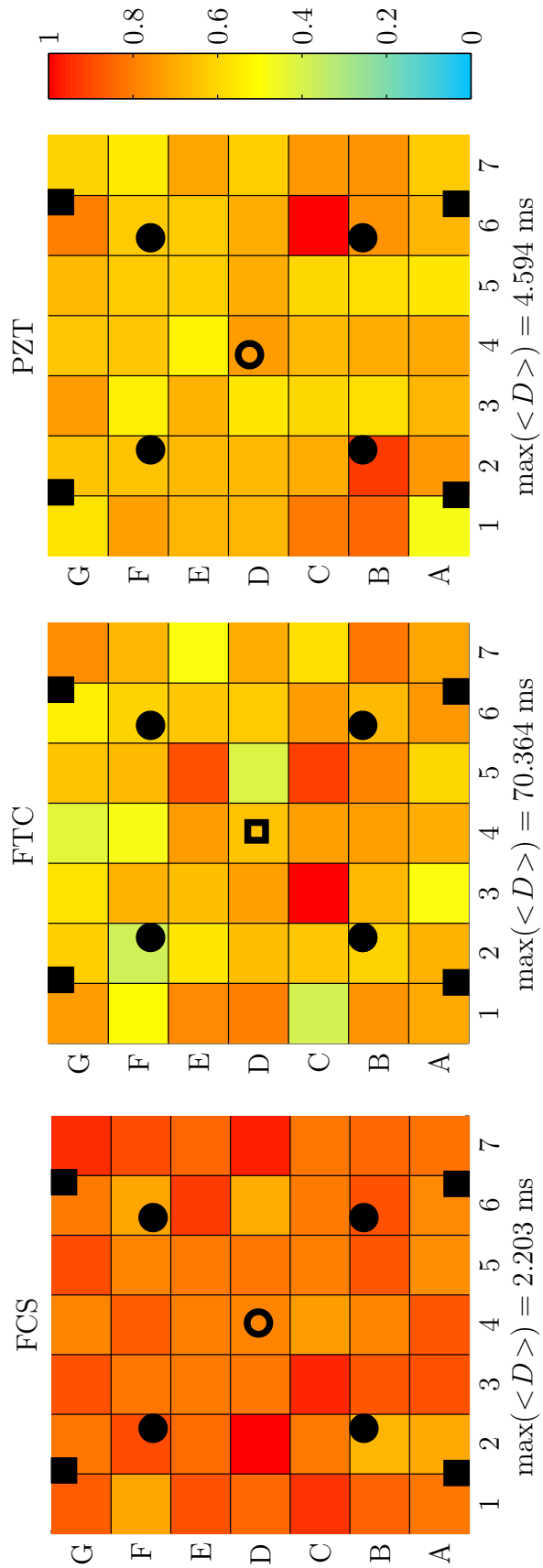

Figure 4.9: Results of $< D > / \max(< D >)$ parameter with sensors at center hole.

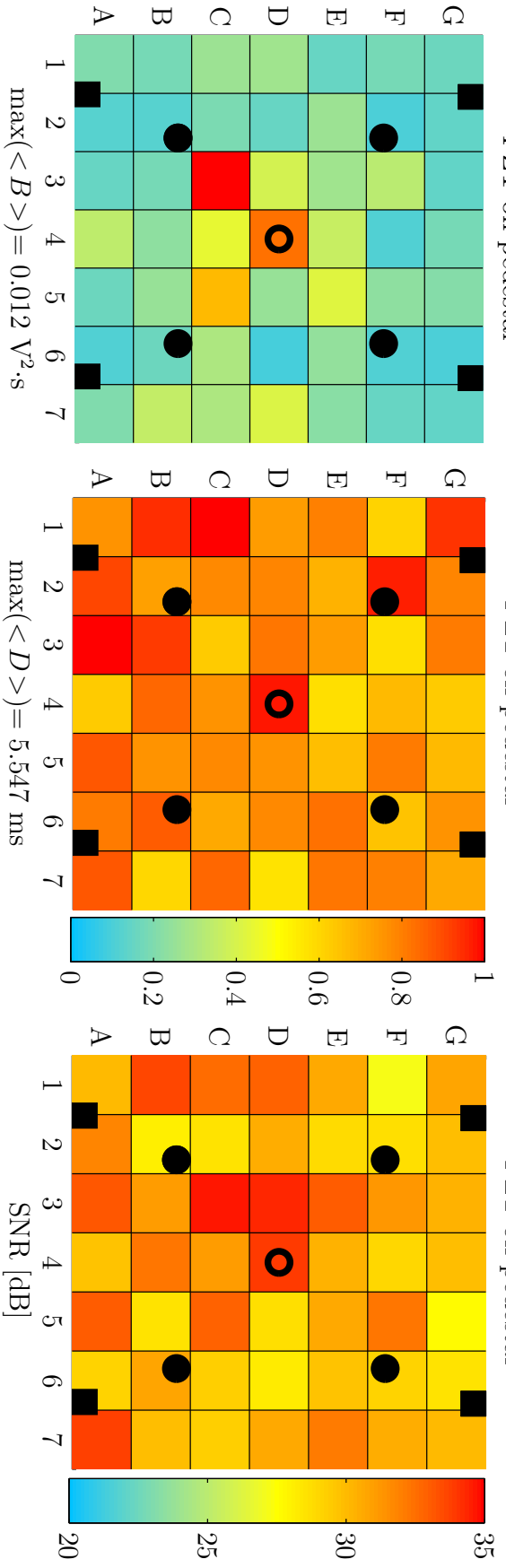

Figure 4.10: Results of parameter of PZT on pedestal at center hole.

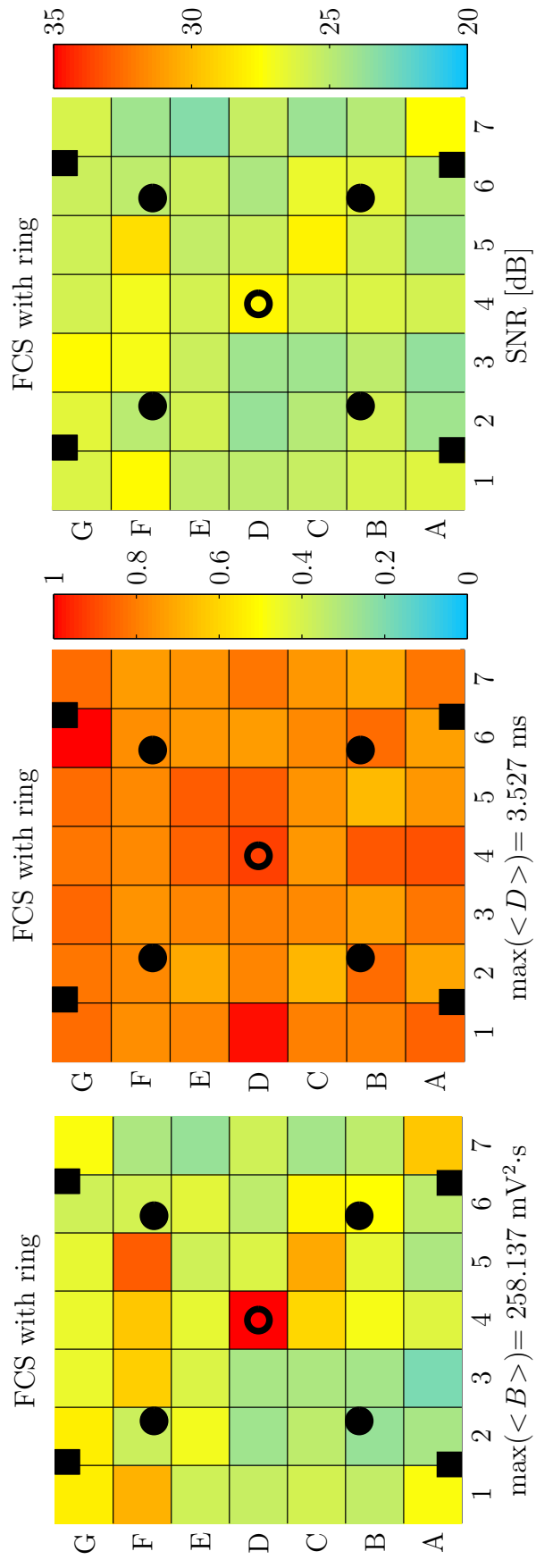

Figure 4.11: Results of parameter of FCS with ring at center hole.

Chapter 5

Conclusions

In this thesis we have characterized two optic fiber sensors for landslides monitoring. Two fiber coil sensors (FCSs) have been preliminary characterized in term of responsivity and SNR, with respect to pressure and acceleration. Both FCS have shown good sensitivity to acceleration and the mandrel-type FCS have shown promising performance also with respect to pressure.

Along with the mandrel-type FCS we have considered another interferometric sensor (namely a "ferrule top cantilever", FTC) consisting in a micro cantilever carved on the top of a cylindrical silica ferrule; both sensors have been compared with a standard piezoelectric transducer (PZT). Taking into account the differences in electrical amplification, the most sensitive sensor is the FTC, although FTC is also the one with the least temporal resolution. Experimental results suggest also that FOSs (FTC, in particular) may likely be intrinsically more sensitive to volumes waves (PZT, on the contrary is intrinsically more sensitive to surface waves). To the aim of rock mass monitoring, this characteristic of the FOSs is indeed desirable, because surface waves are more easily triggered by environmental noise. Even if the PZT outperforms the two FOSs in sensitivity, both suggest promising feature for this field of application.

Appendix A

Acoustic insulation of sensors

The acoustic insulation of FCS with respect to external sources is important during the measurement in laboratory, to reduce the noise, but also in field to avoid false alarm. We report here the results obtained using four different material: a gray, white and a pink type of polystyrene, and a white expanded polystyrene. A vertical buzzer driven by a 10 V_{pp} sinusoidal signal generates pressure waves directed to the PZT, as shown in Figure A.1. An hollow cylinder of pink polystyrene, placed in between, is used to isolate source and receiver form external noise. Then a layer of insulator is inserted in between the PZT and the source and the change of intensity of the signal is measured for different acoustic frequencies (see bottom-right photo of Figure A.1).

Signal intensity and SNR, resulting from signals recorded manually, are reported in Figure A.2 and show that the white expanded polystyrene provides the best acoustic isolation in the frequency range of our interest, because it has the lowest responsivity along with negative SNR.

For the package built for the Mandrel FCS, another test has been realized. In this case the same gray polystyrene covers all the Mandrel and the same setup used for pressure responsivity was used. Results, not reported for brevity, show a mean responsivity of -65 dBV and negative SNR for all frequency range. This difference in frequency respond between this case and the previous one comes from the different sensitivity of the sensors used and the complete covering of the Mandrel.

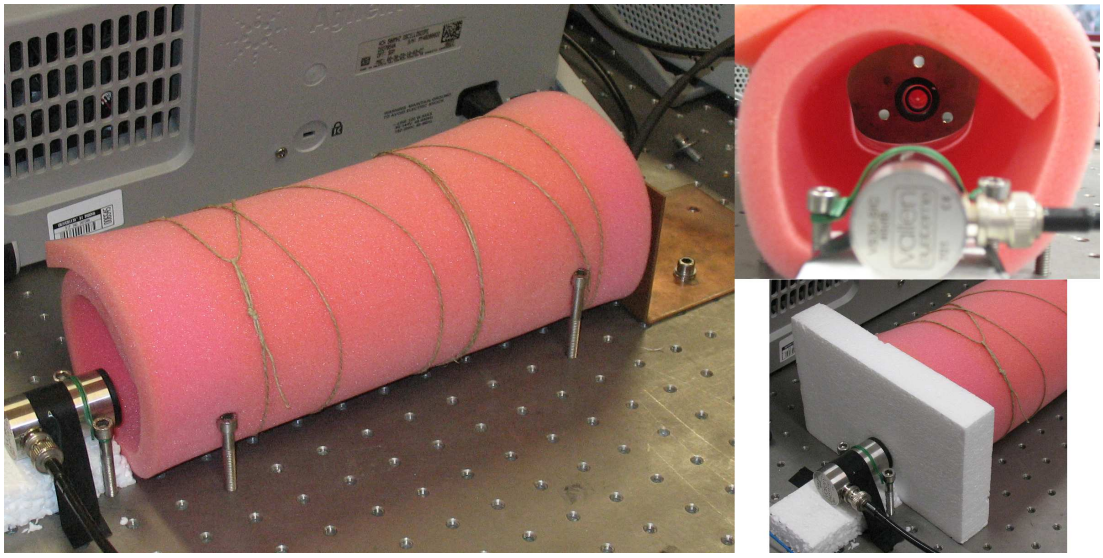

Figure A.1: Setup of acoustic insulation test.

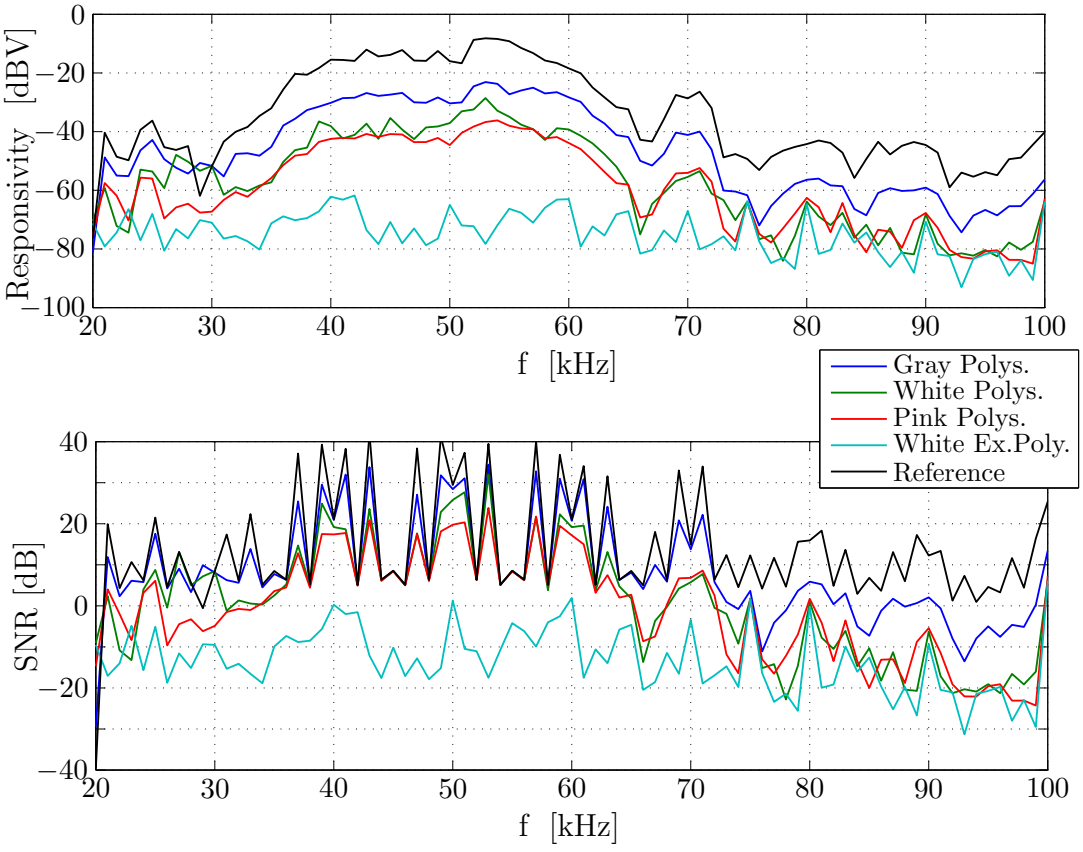

Figure A.2: Results of acoustic insulation.

References

[1] K.C. Kao and G.A. Hockham. Dielectric-fibre surface waveguides for optical frequencies. *Optoelectronics, IEE Proceedings J*, 133(3):191 –198, june 1986.

[2] B. Culshaw and A. Kersey. Fiber-optic sensing: A historical perspective. 26(9):1064–1078, 2008.

[3] G. Wild and S. Hinckley. Acousto-ultrasonic optical fiber sensors: Overview and state-of-the-art. *Sensors Journal, IEEE*, 8(7):1184 –1193, 2008.

[4] K. Kageyama, H. Murayama, K. Uzawa, I. Ohsawa, M. Kanai, Y. Akematsu, K. Nagata, and T. Ogawa. Doppler effect in flexible and expandable light waveguide and development of new fiber-optic vibration/acoustic sensor. *IEEE/OSA Journal of Lightwave Technology*, 24(4):1768–1775, 2006.

[5] T. Giallorenzi, J. Bucaro, A. Dandridge, G. Sigel, J. Cole, S. Rashleigh, and R. Priest. Optical fiber sensor technology. 18(4):626–665, 1982.

[6] O. Strobel, D. Seibl, J. Lubkoll, and R. Rejeb. Fiber-optic sensors - an overview. In *Proc. 11th Int. Conf. Transparent Optical Networks ICTON '09*, pages 1–6, 2009.

[7] G. Manthei, J. Eisenblatter, and T. Spies. *Acoustic Emission in Rock Mechanics Studies in Acoustic Emission - Beyond the Millennium.* Elsevier, 2000.

[8] N. J. Rosser, M. Lim, D. N. Petley, S. Dunning, and R. J. Allison. Patterns of precursory rockfall prior to slope failure. *Journal of geophysical research : earth surface.*, 112:F04014, November 2007.

[9] Z. Chen and F. Ansari. Fiber optic acoustic emission distributed crack sensor for large structures. *Journal of Structural Control*, 7(1):119–129, 2006.

[10] Yuichi Machijima, Seiji Kikuyama, Masahiro Tanaka, and Tsuyoshi Ishida. Application of fiber-optic doppler sensor to rock structures. In *Proc. 2nd International Conference on Structural Condition Assessment, Monitoring and Improvement*, pages 888–892, 2007.

[11] G. Gautschi. *Piezoelectric sensorics: force, strain, pressure, acceleration and acoustic emission sensors, materials and amplifiers*. Engineering online library. Springer, 2002.

[12] G Gruca, S de Man, M Slaman, J H Rector, and D Iannuzzi. Ferrule-top micromachined devices: design, fabrication, performance. *Measurement Science and Technology*, 21(9):094033, 2010.

[13] N. Carino. The impact-echo method: an overview. In *Proceedings of the 2001 Structures Congress & Exposition*. American Society of Civil Engineers, 2001.

Acknowledgements

Vorrei ringraziare prima di tutto la mia famiglia, Roberto, Anna e Stefano per tutto il sostegno datomi in questi anni di studio.

Un ringraziamento speciale al Professor Luca Palmieri per la possibilità di lavorare in questo progetto, e all' Ing. Luca Schenato per tutta la professionalità e pazienza con cui mi ha aiutato a sviluppare questa tesi in questi mesi di laboratorio. Come non ringraziare poi Elena e Fabrizio per la loro disponibilità e aiuto in laboratorio, e gli altri tesisti del gruppo di Fotonica con cui ho trascorso questi mesi.

Un grazie poi a tutti i pendolari che hanno vissuto con me i viaggi in treno (anche se spesso dormivo...), a tutti i veneziani che spesso mi sopportano e supportano spiritualmente, e infine a tutti i padovani di nascita o di acquisizione conosciuti in questi anni di università.

Leonardo